Received: 28 December 2017 | Revised: 17 April 2018 | Accepted: 25 April 2018
DOI: 10.1111/jmg.12423

ORIGINAL ARTICLE

WILEY Journal of METAMORPHIC GEOLOGY

Tectonometamorphic evolution of the Atbashi high-*P* units (Kyrgyz CAOB, Tien Shan): Implications for the closure of the Turkestan Ocean and continental subduction–exhumation of the South Kazakh continental margin

Chloé Loury[1] | Yann Rolland[1,2] | Stéphane Guillot[2] | Pierre Lanari[3] | Clément Ganino[1] | Raphael Melis[1] | Anthony Jourdon[1] | Carole Petit[1] | Olivier Beyssac[4] | Sylvain Gallet[1] | Patrick Monié[5]

[1]Université Côte d'Azur, CNRS, OCA, IRD, Valbonne, France
[2]Univ. Grenoble Alpes, Univ. Savoie Mont-Blanc, CNRS, IRD, IFSTTAR, Grenoble, France
[3]Institute of Geological Sciences, University of Bern, Bern, Switzerland
[4]Institut de Minéralogie, de Physique des Matériaux, et de Cosmochimie (IMPMC), UMR CNRS, Sorbonne Universités – UPMC Univ Paris 06, Paris, France
[5]Géosciences Montpellier, UMR 5243, Université Montpellier, Montpellier, France

Correspondence
Yann Rolland, Université Côte d'Azur, CNRS, OCA, IRD, Valbonne, France.
Email: yrolland@unice.fr

Funding information
ANR, Grant/Award Number: ANR-13-BS06-012-01

Handling Editor: Doug Robinson

Abstract
The South Tien Shan (STS) belt results from the last collision event in the western Central Asian Orogenic Belt (CAOB). Understanding its formation is of prime importance in the general framework of the CAOB. The Atbashi Range preserves high-*P* (HP) rocks along the STS suture, but still, its global metamorphic evolution remains poorly constrained. Several HP units have been identified: (a) a HP tectonic mélange including boudins of mafic eclogites in a sedimentary matrix, (b) a large (>100 km long) high-*P* metasedimentary unit (HPMU) and (c) a lower blueschist facies accretionary prism. Raman Spectroscopy on carbonaceous material combined with phengite and chlorite multiequilibria and isochemical phase diagram modelling indicates that the HPMU recorded homogeneous *P*–*T* conditions of 23–25 kbar and 560–570°C along the whole unit. $^{40}Ar/^{39}Ar$ dating on phengite from the HPMU ranges between 328 and 319 Ma at regional scale. These ages are interpreted as (re-) crystallization ages of phengite during T_{max} conditions at a pressure range of 20–25 kbar. Thermobarometry on samples from the HP tectonic mélange provides similar metamorphic peak conditions. Thermobarometry on the blueschist to lower greenschist facies accretionary prism indicates that it underwent *P*–*T* conditions of 5–6 kbar and 290–340°C, highlighting a 17–20 kbar pressure gap between the HPMU-tectonic mélange units and the accretionary prism. Comparison with available geochronological data suggests a very short time span between the prograde path (340 Ma), HP metamorphic peak (330 Ma), the T_{max} (328–319 Ma) and the final exhumation of the HPMU (303–295 Ma). Extrusion of the HPMU, accommodated by a basal thrust and an upper detachment, was driven by buoyant forces from 70–75 km up to 60 km depth, which directly followed continental subduction and detachment of the HPMU. At crustal depths, extrusion was controlled by collisional tectonics up to shallow levels. Lithological homogeneity of the HPMU and its continental-derived character from the North Tien Shan suggest this unit corresponds to the hyper-extended continental margin of the Kazakh continent, subducted southward below the north

continental active margin of the Tarim craton. Integration of the available geological data allows us to propose a general geodynamic scenario for Tien Shan during the Carboniferous with a combination of (a) N-dipping subduction below the Kazakh margin of Middle Tien Shan until 390–340 Ma and (b) S-dipping subduction of remaining Turkestan marginal basins between 340 and 320 Ma.

KEYWORDS

Central Asian Orogenic Belt, continental subduction, HP metamorphism, *P–T–t* history, South Tien Shan

1 | INTRODUCTION

High-pressure–low temperature (HP–LT) metamorphism is an important witness of subduction zone dynamics. Detailed study of HP-UHP units combining structural, geochemical, petrological and petrochronological analyses is used for understanding palaeo-subduction dynamics and history (e.g., Engi, Lanari, & Kohn, 2017) and regional geodynamic evolution. The study of HP–LT metamorphism of accretionary orogens is often complicated by the collage of multiple (micro-) blocks and the subduction of numerous oceanic domains (e.g., Cawood et al., 2009; Xiao et al., 2014). The South Tien Shan (STS) range in Central Asia results from the docking of the Tarim craton with the Kazakh block or platform (Figure 1a) after the final closure of the Turkestan Ocean in the Late Carboniferous (e.g., Biske, 1995; Charvet et al., 2011). This is the final accretion event recorded in the western part of the Central Asian Orogenic Belt (CAOB; e.g., Kröner et al., 2017; Windley, Alexeiev, Xiao, Kroner, & Badarch, 2007), before a new subduction initiated south of the Tarim craton with the closure of the Paleo-Tethys Ocean (e.g., Metcalfe, 2013). Constraining the geodynamic evolution of the STS is, thus, important for understanding the final stages of CAOB collisional history. However, numerous models have been recently proposed, which disagree in terms of timing and subduction polarity (see Section 2). HP–LT metamorphism along the STS suture zone occurs both in Kyrgyzstan (Atbashi Range) and in western China (Akeyazi area). Previous studies on the Kyrgyz Atbashi Range (Figure 1b,c) mainly focused on mafic eclogites, and details regarding the spatial extent and timing of HP metamorphism within the associated metasedimentary rocks and lower grade metamorphic stages at the scale of the Tien Shan belt are still lacking (Hegner et al., 2010; Loury, Rolland, Cenki-Tok, Lanari, & Guillot, 2016; Loury et al., 2015; Simonov, Sakiev, Volkova, Stupakov, & Travin, 2008). Therefore, following these previous works, the main questions addressed in this paper are: (a) what was the timing of burial and exhumation in the Atbashi Range? and (b) what is the geodynamic significance of this HP metamorphism for the western CAOB history?

The aim of this paper is, thus, to investigate the overall metamorphic history of the Atbashi Range in Kyrgyzstan (Figure 1) by constraining its metamorphic evolution at a regional scale (i.e., all along its >100 km length). Two metamorphic domains are investigated for their metamorphic evolution: (a) the HP (eclogite facies) units and (b) the accretionary prism LP–MP units. To do this, samples were collected in several transects all along the Atbashi Range (Figure 1b,c). Further, a detailed geochemical, petrological, thermobarometric and $^{40}Ar/^{39}Ar$ geochronological study was conducted to compare the evolution of the *P–T–t* conditions of the different tectonic units. These data are used to constrain the evolution of the HP prism and give insights into the western CAOB metamorphic history.

2 | GEOLOGICAL SETTING

2.1 | The Tien Shan

The Tien Shan Belt is located in the southwestern part of the CAOB and extends for more than 2,000 km from Uzbekistan to western China. It was formed during the Palaeozoic, following amalgamation of several tectonic blocks (Kröner et al., 2014, 2017; Sengör, Natalin, & Burtman, 1993; Wilhem, Windley, & Stampfli, 2012; Windley et al., 2007; Xiao, Huang, Han, Sun, & Li, 2010). During Cenozoic times, the belt was reactivated following the India-Asia collision forming the present-day high-relief (e.g., Jolivet et al., 2010; Molnar & Tapponnier, 1975; Sobel, Oskin, Burbank, & Mikolaichuk, 2006). In Kyrgyzstan, the Tien Shan belt is classically divided into three main units: the North, Middle and South Tien Shan (NTS, MTS and STS, respectively, Figure 1a) (e.g., Bakirov & Maksumova, 2001; Nikolaev, 1933). The Kyrgyz NTS and MTS were amalgamated in the early Palaeozoic (e.g., Alexeiev et al., 2011; Kröner et al., 2013, 2017; Mikolaichuk, Kurenkov, Degtyarev, & Rubstov, 1997). In the Late Carboniferous, the Tarim craton was accreted to the MTS

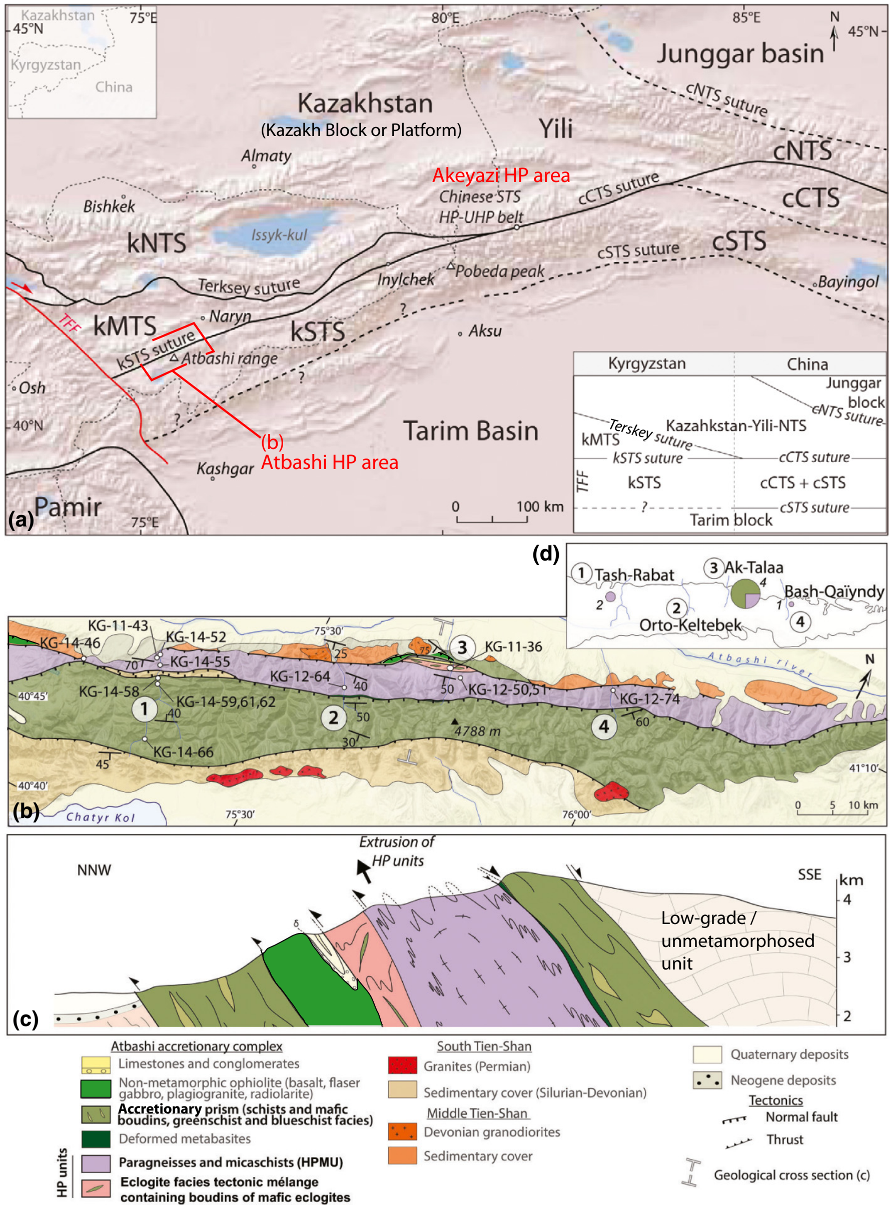

FIGURE 1 (a) Tectonic sketch of the Tien Shan belt (western part of the CAOB) showing the location of the Atbashi range enlarged map (b) (modified after Loury et al., 2015). Insert: tectonic sketch the main sutures and blocks of the western CAOB. (b) Geological map of the Atbashi Range showing location of samples of this study. (c) Cross-section of the Atbashi range along the Ak-Talaa valley, modified after Loury et al. (2015) and Jourdon, Petit, et al. (2017). Numbered circles refer to the valley names indicated in (d). (d) Name of the different valleys and relative proportion of metamorphic studies (illustrated by the relative size of coloured circles and number in italic) highlighting the need of a study at the scale of all the Atbashi range (coloured circles: green for mafic eclogites and purple for HPMU). kNTS, Kyrgyz North Tien Shan; kMTS, Kyrgyz Middle Tien Shan; kSTS, Kyrgyz South Tien Shan; cNTS, Chinese North Tien Shan; cCTS, Chinese Central Tien Shan; cSTS, Chinese South Tien Shan; TFF: Talas Ferghana Fault

following closure of the Turkestan Ocean (also referred as Paleo-Asian, STS, or Central Tien Shan, ocean), which resulted in the formation of the STS fold-and-thrust belt (Biske, 1995; Hegner et al., 2010). HP–LT metamorphism has been described along the STS suture zone in the Atbashi Range in Kyrgyzstan and in the Akeyazi area in western China (Figure 1a; e.g., Gao & Klemd, 2003; Hegner et al., 2010; Meyer, Klemd, John, Gao, & Menneken, 2016; Tagiri, Yano, Bakirov, Nakajima, & Uchiumi, 1995; van der Straaten, Schenk, John, & Gao, 2008; Wang et al., 2009). In the Atbashi Range, the palaeo-subduction complex is well preserved with the presence of a HP tectonic mélange containing mafic eclogites and a HP metasedimentary unit (HPMU) exhumed within a palaeo-accretionary prism (Figure 1b–d). According to the vergence of structures along the STS, to the east of the Talas Ferghana Fault, extrusion of the HPMU was accommodated by a basal (top-to-the-north) thrust and an upper (top-to-the-south) detachment (Figure 1b), which suggests that the subduction of the Turkestan Ocean was south-dipping (e.g., Charvet et al., 2011; Loury et al., 2015). This south-dipping subduction is also suggested by the opening of back-arc basins along the N-Tarim margin (upper plate) at 334–309 Ma (Wang et al., 2017; Zhong et al., 2017). In contrast, to the west of the Talas Ferghana Fault, a nappe stack includes *c.* 315 Ma eclogite boudins, dated at 301 ± 15 Ma by U–Pb on allanite by Loury et al. (2016) and to 317 ± 4 Ma and 316 ± 3 Ma by Sm–Nd garnet whole-rock ages (Mühlberg et al., 2016), suggesting a north-dipping subduction (Loury et al., 2016). Thermo-mechanical modelling of the STS belt is in agreement with a south-dipping subduction model (Jourdon, Le Pourhiet, Petit, & Rolland, 2017), at least at the end of the Turkestan Ocean closure history. These models show that the Cenozoic development of top-to-the-north thrusts along the STS necessitates an originally south-dipping crustal structure. However, the crustal-scale used in the thermo-mechanical models does not permit the reproduction of the detailed structural evolution of the STS at the scale of studied metamorphic units, and to include all their rheological complexity (serpentinized layers, continental units, metasedimentary rocks, etc.). Alternative tectonic models proposed north-dipping subduction, mainly based on the current structure of STS belt, which is thrust towards the south onto the Tarim basin (e.g., Makarov et al., 2010; Windley, Allen, Zhang, Zhao, & Wang, 1990), but most of these top-to-the-south thrusts are Cenozoic in age (Jourdon, Le Pourhiet, et al., 2017). In the alternative north-dipping subduction scenario, arc-magmatism dated at 390–340 Ma in the Central Tien Shan—Yili Block (Gao et al., 2009; Han, He, Wang, & Guo, 2011; Han et al., 2016; Konopelko, Seltmann, Biske, Lepekhina, & Sergeev, 2009; Seltmann, Konopelko, Biske, Divaev, & Sergeev, 2011) could be related to the north-dipping subduction. This hypothesis seems to be supported by the scarcity of arc-magmatic events on the southern side of the Turkestan ocean, as investigated Palaeozoic clastic rocks in the STS and in the northern Tarim craton margin contain very little Devonian–Carboniferous detrital zircon (Han & Zhao, 2017). In this paper, we argue for a model which combines a long-lived (390–340 Ma) north-dipping subduction of this oceanic lithosphere below MTS, followed by a short-lived (340–320 Ma) subduction below the Tarim craton. After this long period of subduction, a transition towards a transcurrent tectonic regime throughout the CAOB accommodated rotations of different blocks in the Tien Shan with respect to Siberia and Tarim cratons, during the Late Carboniferous to Early Permian (Allen & Vincent, 1997; Allen, Windley, & Zhang, 1992; Jourdon, Petit, et al., 2017; Laurent-Charvet, Charvet, Monié, & Shu, 2003; Rolland et al., 2013; Wang et al., 2007). Coeval with this wrench tectonics, widespread intracontinental magmatism affected the Tien Shan belt and the northern margin of the Tarim craton.

2.2 | The Atbashi Range

The Atbashi Range is located within the STS, to the east of the Talas-Ferghana Fault (Figure 1). It extends on more than 125 km along the STS suture zone (Figure 1a). To the north, the range is thrust onto the Atbashi Basin along a Cenozoic thrust (Figure 1b; Tursungaziev & Petrov, 2008).

2.2.1 | Geological units

The Atbashi Range constitutes a palaeo-subduction prism represented by different structural units described from north to south along the Ak-Talaa Valley (Figure 1b–d) (Alekseev, Aristov, & Degtyarev, 2007; Bakirov, 1978; Bakirov & Kotov, 1988; Biske, Zubtov, & Porshnyakov, 1985; Hegner et al., 2010; Loury et al., 2015; Sang et al., 2016, 2017):

1. An accretionary prism: This prism is composed of metapelites and calcschists locally including lenses of metabasites and is overthrust onto the MTS sedimentary series.
2. A dismembered nonmetamorphic ophiolite composed of pillow-basalts, flaser gabbros, plagiogranites, serpentinites and cherts: This ophiolite constitutes a fragment of the oceanic lithosphere overthrust towards the north onto the accretionary prism. Conodonts in cherty sequences constrained the age of the ophiolite as Early to Late Devonian (Pragian to Famennian; Alekseev et al., 2007).
3. An eclogite facies tectonic mélange (“HP mélange”) containing decametre-scale mafic eclogitic boudins within a metasedimentary matrix: It was overthrust onto the ophiolite in the Ak-Talaa area. This unit is interpreted as the deepest part of the exhumed accretionary prism (Loury et al., 2015).
4. A metasedimentary unit, made of micaschists and paragneisses (the HPMU): This unit also underwent eclogite facies metamorphism (Loury et al., 2015). In the Ak-Talaa area, it is thrust over the eclogite facies sedimentary mélange, whereas in other places, it is thrust over the MTS sedimentary series. At the top, this unit is bounded by a top-to-the-South detachment underlined by strongly deformed mafic rocks (Loury et al., 2015).
5. The accretionary prism unit, which appears also in the upper structural position in the Ak-Talaa area (Figure 1b,c), is also in contact with the HPMU along the top-to-the-South detachment. This unit underwent low-grade metamorphism and an intense polyphase deformation resulting in folding and development of a NE–SW schistosity dipping towards the north or south (Jourdon, Petit, et al., 2017).
6. The uppermost unit is constituted of low-grade to unmetamorphosed sedimentary rocks, Silurian to Devonian in age (based on the occurrence of Tabulata corals), and is mainly composed of limestones, shales and sandstones (Biske et al., 1985). In some places, as in the Tash-Rabat Valley, the limestones are metamorphosed, as suggested by the presence of marbles, but metamorphic conditions are unconstrained.

2.2.2 | HP metamorphism and geochronology

Mafic eclogite boudins from the HP mélange that crop out in the Ak-Talaa area have been the main focus of the Atbashi range studies (Figure 1d; e.g., Hegner et al., 2010;

Loury et al., 2015; Sang et al., 2017; Simonov et al., 2008; Tagiri et al., 1995). These fragments of mafic eclogites are derived from an oceanic crust with N-MORB and oceanic island basalt (OIB) protoliths (Simonov et al., 2008). The peak conditions reached by the mafic eclogites were estimated at 20–25 kbar and 500–570°C (Hegner et al., 2010; Loury et al., 2015; Simonov et al., 2008; Tagiri et al., 1995). Udovkina (1985) reported the first age estimate for this HP stage with K–Ar dates between 320 and 288 Ma. Tagiri et al. (1995) measured a garnet, omphacite, phengite Rb–Sr isochron age of 267 ± 5 Ma. However, the meaning of these ages remains unclear, as it could reflect partial resetting during the Permian deformation phase (e.g., Loury et al., 2018). More recently, Hegner et al. (2010) obtained a well-defined Sm–Nd isochron age of 319 ± 4 Ma (on omphacite, glaucophane, garnet core and rim, whole rock) for the HP metamorphism and a similar within error $^{40}Ar/^{39}Ar$ plateau age on phengite of 316 ± 3 Ma, which they interpreted as a cooling age. Simonov et al. (2008) obtained $^{40}Ar/^{39}Ar$ plateau ages between 327 and 324 Ma on phengite and glaucophane, also interpreted as cooling ages. The calcic metasedimentary rocks hosting the mafic eclogites underwent similar peak pressure conditions, at 20–21 kbar and slightly lower temperature conditions between 450 and 480°C (Loury et al., 2015). This difference in temperature could either reflect a difference in the timing of re-equilibration of units having different bulk rock compositions along the same *P*–*T* loop, or slightly different *P*–*T* trajectories in agreement with the mélange character of this unit.

The *P*–*T* conditions for the HPMU were estimated, from a mafic sample east of the Atbashi Range (Bash-Qaïyndy valley, Figure 1b,d), at 19 ± 2.5 kbar and 525 ± 50°C (Loury et al., 2015). Hegner et al. (2010) constrained the depositional age of the paragneiss protoliths as younger than 427 Ma and concluded that they could be the high-grade equivalents of the low-grade Silurian–Devonian metasedimentary rocks exposed in the southern part of the Atbashi Range. The abundance of inherited zircon with ages ranging between 450 and 430 Ma in the HPMU led Hegner et al. (2010), Rojas-Agramonte et al. (2014) and Sang et al. (2017) to conclude that their source provenance lies in the North Tien Shan, where 450–430 Ma batholiths are widespread. Rojas-Agramonte et al. (2014) dated metamorphic overgrowths of detrital zircon from a paragneiss of the Tash-Rabat valley (west of the Atbashi Range, Figure 1d) and obtained two U–Pb ages of 336 ± 6 Ma and 329 ± 5, while Sang et al. (2017) obtained zircon overgrowth ages as young as *c*. 250 Ma.

The work carried out so far on the HP metamorphism units of the Atbashi range was thus focused on a few specific areas such as the Ak-Talaa valley (Figure 1d) and on representative lithologies sampled in moraines (Hegner et al., 2010). In order to have a global understanding of the geodynamic evolution of the range during the Late Palaeozoic, a petrochronological study based on structurally constrained sampling has been undertaken at the scale of the whole Atbashi range and is described in the following.

3 | RESULTS

3.1 | HP tectonic melange

The sampling strategy and analytical procedures are fully described in Appendix S1. The eclogite sample KG-11-36 was collected in a decametre scale elongated mafic boudin embedded in a metasedimentary matrix (Loury et al., 2015). Both the hosting metasedimentary rocks and metamafic boudins underwent eclogite facies metamorphism during the late Carboniferous oceanic subduction. For more field and structural description, the reader is referred to Loury et al. (2015).

3.1.1 | Sample description

The sample contains ~50 vol.% of garnet. The remaining 50 vol.%, so-called matrix, is mainly made of omphacite (47 vol.%) and rutile (3 vol.%; Figures S1 and S2). Garnet occurs as euhedral porphyroblasts (1–3 mm) containing up to 40 vol.% of inclusions of omphacite, rutile, quartz and minor glaucophane and phengite. Glaucophane and phengite are only observed in one garnet core (Figure 2). Towards the rim (from Garnet 1 to Garnet 3, Figure 2, see below Section 3.1.2), glaucophane is progressively replaced by omphacite inclusions, while phengite is absent. Quartz inclusions form a corona in the garnet zone Grt2a. This inclusion pattern suggests that garnet records evidence from successive growth stages with different metamorphic assemblages reflecting different *P*–*T* conditions. Glaucophane and phengite of the garnet core are the only hydrous phases found in this eclogite suggesting that the rock was progressively dehydrated during the garnet growth. The garnet porphyroblast with glaucophane and phengite inclusions (Figure S1) was selected for further investigations by high-resolution quantitative X-ray micro-mapping (e.g., Lanari, Vho, Bovay, Airaghi, & Centrella, 2018; Lanari et al., 2014). The occurrence of both glaucophane and phengite in the garnet core suggests that it represents an earlier upper blueschist facies stage of growth (Figure 2).

3.1.2 | Compositional groups of garnet and omphacite

Garnet has been divided into three zones (Grt1, Grt2, Grt3; Figure 2) based on (a) relatively homogeneous compositions at the scale of each zone and (b) on the nature and composition of inclusions contained in each zone (Figure 2; Figures S1 and S2 and Tables S2–S6).

1. The first zone corresponds to the garnet core (Grt1), which has the composition $Alm_{64}Prp_{11}Grs_{24}Sps_{01}$ and preserves glaucophane, phengite, paragonite, omphacite, quartz and rutile inclusions. The geometry of Grt1 is not a standard garnet crystal shape and does not show any euhedral-granular texture.
2. The second zone is the garnet mantle (Grt2), with the composition: $Alm_{66\text{-}65}Prp_{12\text{-}16}Grs_{21\text{-}18}Sps_1$. The Grt2 composition evolves continuously from the inner to the outer mantle and the nature of inclusions also changes. According to these observations, the garnet mantle was divided into three subzones (Figure 2). The first subzone (Grt2a) or garnet inner mantle has the following composition: $Alm_{66}Prp_{12}Grs_{21}Sps_1$, and includes the quartz corona. In addition, it hosts some omphacite, glaucophane and rutile inclusions. The second subzone (Grt2b) corresponds to the central part of the garnet mantle showing a composition of $Alm_{66}Prp_{13}Grs_{20}Sps_1$. Omphacite and rutile inclusions are still preserved in this subzone. The third subzone (Grt2c) is the garnet outer mantle, which has a composition of $Alm_{65}Prp_{16}Grs_{18}Sps_1$ and shows inclusions of omphacite and rutile.
3. The garnet rim (Grt3) shows a sharp change in garnet composition with $Alm_{54}Prp_{25}Grs_{21}$. Omphacite and rutile inclusions are still present.

In some restricted garnet areas (between Grt1 and Grt2a and between Grt2c and Grt3), an irregular contact between adjacent zones and a sharp change in composition may evidence resorption and/or postcrystallization compositional changes of the garnet (e.g., Giuntoli, Lanari, & Engi, 2018). In order to avoid any artefact in the *P–T* estimates, due to some diffusion or replacement process affecting the

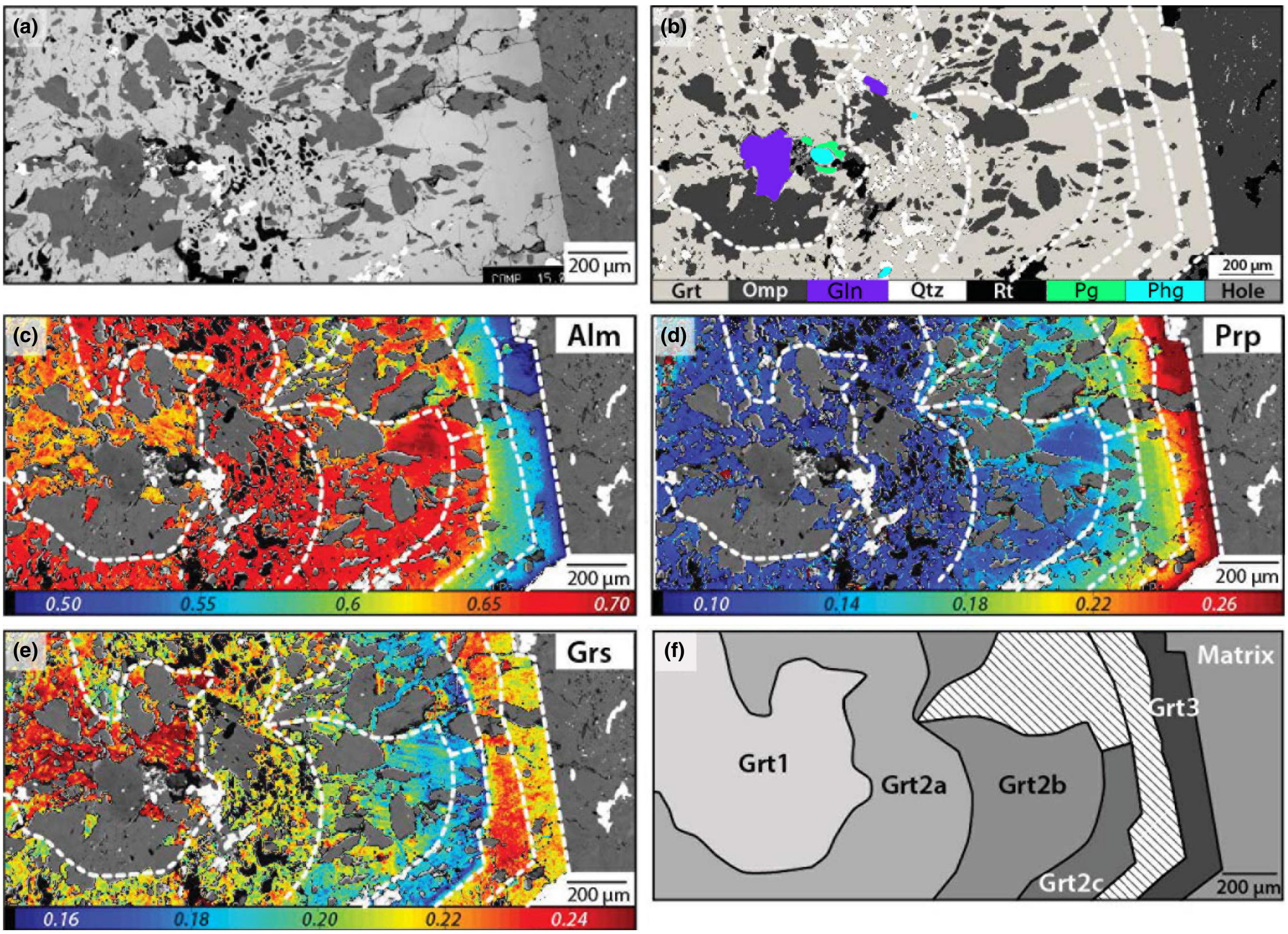

FIGURE 2 Illustrations of the garnet area ("small map") of an eclogite mafic boudin from the "HP Tectonic Mélange" unit (sample KG-11-36, see location of investigated zone on Figure 1 and Figures S1 and S2). The garnet core is to the left side of the figures. (a) BSE image of the mapped area. (b) Identification of phases and different groups (white dashed lines, see the text for explanations of groups distinction). (c–e) Garnet end-member compositional maps (c) Almandine, (d) Pyrope, (e) Grossular and different groups (white dashed lines). (f) Scheme of the studied garnet and its surrounding matrix with the different groups. The hashed area was not investigated due to its heterogeneous nature

garnet composition, these domains have been ignored in further calculations (lined areas in Figure 2f).

Omphacite inclusions in the garnet have a jadeite content of $Jd_{26\text{-}32}$ in Grt1, $Jd_{34\text{-}36}$ in Grt2 and $Jd_{27\text{-}29}$ in Grt3, while the jadeite content of omphacite in the matrix ranges from Jd_{32} in the cores of some grains to Jd_{25} towards their rims. Overall, an increase of the jadeite content is observed from core to rim in omphacite inclusions between Grt1 and Grt2 and a further decrease is observed towards Grt3. However, omphacite inclusions show a complex zoning pattern (Figure S2). For instance, the jadeite content ranges from Jd_{27} to Jd_{36} in a given inclusion of Grt2. Further, in Grt1, an increase from Jd_{26} to Jd_{32} is observed towards the rim, based on two grains of omphacite, while in Grt3, only 20% of the grains show a decreasing trend from Jd_{35} to Jd_{30} from core to rim. Those complex zonings demonstrate that the whole set of inclusions did not reach thermodynamic equilibrium with the growing garnet at the time of the capture. In such case, empirical or semi-empirical garnet–clinopyroxene inverse thermometry should be used with caution, particularly for Grt2.

3.1.3 | Thermobarometry

The *P–T* conditions of growth of the garnet core (Grt1) were determined using classical thermobarometry. The garnet–omphacite thermometer of Ravna (2000) and the garnet–omphacite–phengite barometer of Waters and Martin (1993) and Waters (1996) have been used. The average composition of garnet core, omphacite and phengite in Grt1 was tentatively used to calculate the *P–T* conditions at the onset of garnet growth. The *P–T* conditions of 450 ± 50°C and 17 ± 2 kbar have been obtained, which is consistent with the results of Loury et al. (2015) for the same sample. For the garnet mantle (Grt2) and rims (Grt3), equilibrium phase diagrams were computed using the software Theriak-Domino (de Capitani & Petrakakis, 2010) (Figure 3). The internally consistent thermodynamic data set of Holland and Powell (1998) and subsequent updates (tc55) were used. Isochemical equilibrium phase diagrams were calculated in the MnO–Na_2O–CaO–FeO–MgO–Al_2O_3–SiO_2–H_2O–TiO_2–O (MnNCFMASHTO) system. K_2O was excluded as phengite (<0.5 vol.%) is the only observed K-bearing phase and only one grain was found in the entire thin section. Solid solution models used were those of Holland and Powell (1998) for garnet, Green, Holland, and Powell (2007) for omphacite and Diener, Powell, White, and Holland (2007) for amphibole. The oxygen fugacity was buffered in the models to quartz-fayalite-magnetite (Spear, 1995). The obtained *P–T* conditions for the three domains of Grt2 (a–c) record similar *P–T* conditions of 510 ± 20°C and 25 ± 2 kbar (Figure 3).

The *P–T* conditions of Grt3 growth occurred in anhydrous conditions, as suggested by the absence of any hydrous phases neither included in the garnet rim nor in the matrix. The jadeite content of the omphacite included in Grt3 and in the matrix is Jd28, which is lower than omphacite inclusions in Grt2. This suggests that Grt3 grew at lower pressure and consequently during the retrograde path.

3.2 | HP metasedimentary unit

3.2.1 | Geochemistry

Metasedimentary samples of the HPMU are SiO_2 rich (58–67 wt%) and have a relatively low K_2O content (1–3 wt%). Their major element composition is represented on a ACF diagram (Figure 4a). They are aluminous in agreement with a pelitic protolith. Large Ion Lithophile Elements and light rare earth elements (LREEs) show enrichments with respect to heavy rare earth elements (HREEs) with $(La/Yb)_N$ ratios between 8.6 and 11.1 (Figure 4b). There are also clear negative Nb–Ta anomalies, with $(Nb/La)_N$ ratios between 0.26 and 0.29, and a marked Pb anomaly with $(Pb/Ce)_N$ ratios between 2.6 and 7. These features are representative of the Upper Continental Crust average composition (Rudnick & Gao, 2003).

3.2.2 | Petrology

The HPMU is made of paragneiss (Figures 5b,c and 6d–f), micaschist (Figures 5a,d and 6b,c) and locally quartzite (Figure 6a). Paragneiss has a (very) fine-grained texture. It contains quartz+albite+white mica+chlorite+clinozoisite+garnet±titanite±calcite assemblage. The deformation is characterized at the centimetre scale by intensely folded quartz veins (Figure 5b,c). Garnet porphyroblasts are subidioblastic to xenoblastic and 0.2–1 mm in size (Figure 6d,f). Chlorite replaced garnet at the grain rims and sometimes totally, resulting in garnet pseudomorphs (Figure 6d). White mica is idioblastic to subidioblastic and 0.3–3 mm in length (Figure 6b,d–f).

Micaschist has a very fine-grained texture and has a quartz+albite+white mica+chlorite+clinozoisite±titanite±calcite assemblage. It is intensely deformed, with a composite HP foliation of white mica and chlorite (Figure 6c). Phengite occurs as 0.1–1 mm long flakes. Albite grains are millimetre-sized and contain inclusions of phengite, chlorite and clinozoisite (Figure 6c). These inclusions are oriented parallel to matrix foliation indicating that albite is postkinematic, which is a typical texture of retrograde albite.

Quartzite occurs to the west in the Tash-Rabat valley. It consists of a quartz+albite+white mica+chlorite±titanite assemblage. A weak foliation is underlined by elongated chlorite aggregates and white mica, which occurs as 0.1–0.5 mm in length grains (Figure 6a).

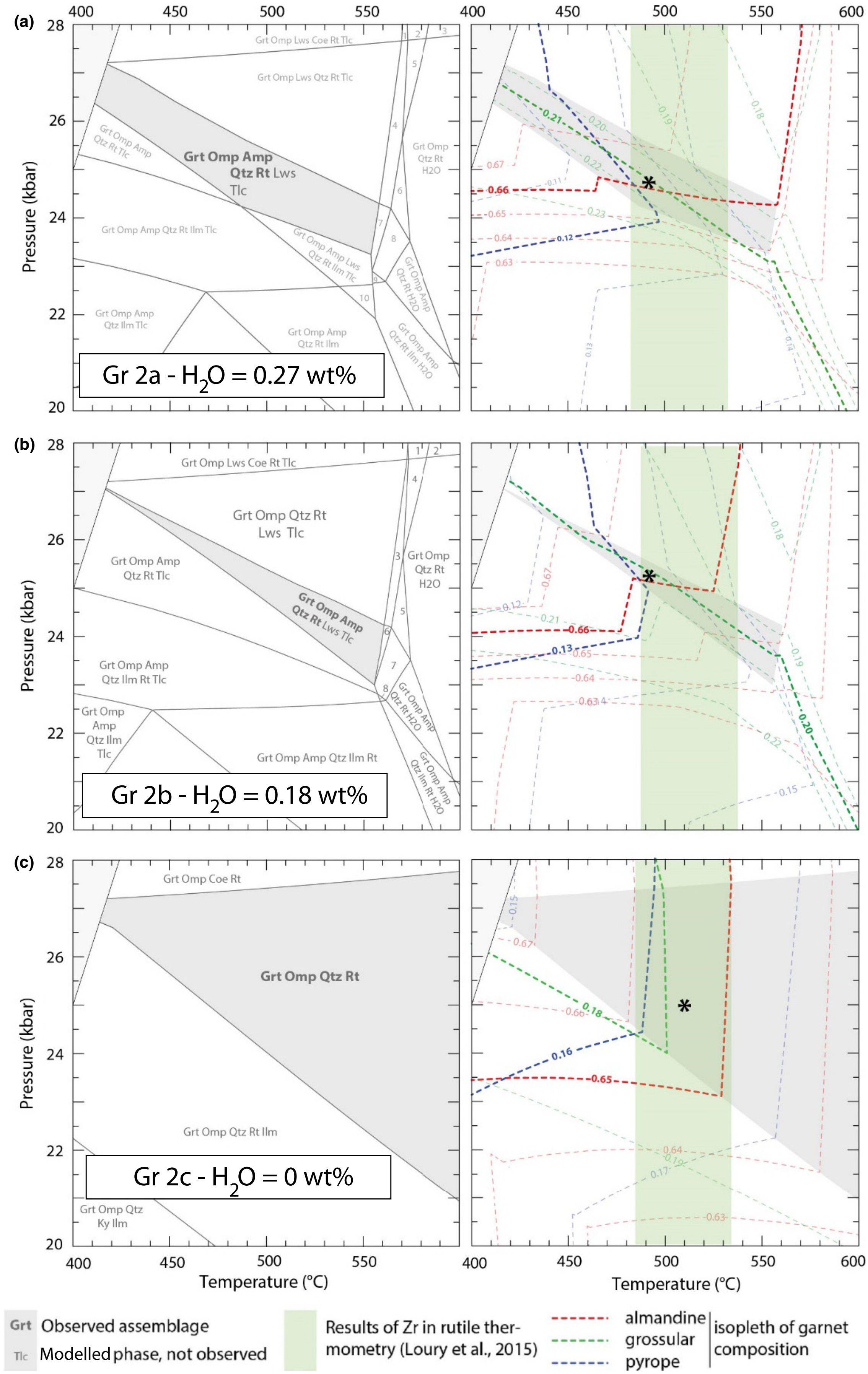
(a)
(b)
(c)
Pressure (kbar)
Temperature (°C)
Grt Omp Lws Coe Rt Tlc
Grt Omp Lws Qtz Rt Tlc
Grt Omp Amp Qtz Rt Tlc
Grt Omp Amp Qtz Rt Lws Tlc
Grt Omp Qtz Rt H2O
Grt Omp Amp Qtz Rt Ilm Tlc
Grt Omp Amp Lws Qtz Rt Ilm Tlc
Grt Omp Amp Qtz Rt H2O
Grt Omp Amp Qtz Ilm Tlc
Grt Omp Amp Qtz Rt Ilm
Grt Omp Amp Qtz Rt Ilm H2O
Gr 2a - H_2O = 0.27 wt%
Grt Omp Qtz Rt Lws Tlc
Grt Omp Amp Qtz Ilm Rt Tlc
Grt Omp Amp Qtz Ilm Tlc
Grt Omp Amp Qtz Ilm Rt
Gr 2b - H_2O = 0.18 wt%
Grt Omp Coe Rt
Grt Omp Qtz Rt
Grt Omp Qtz Rt Ilm
Grt Omp Qtz Ky Ilm
Gr 2c - H_2O = 0 wt%
Grt Observed assemblage
Tlc Modelled phase, not observed
Results of Zr in rutile thermometry (Loury et al., 2015)
almandine
grossular
pyrope
isopleth of garnet composition

FIGURE 3 *P–T* phase equilibria diagram of an eclogite mafic boudin from the "HP Tectonic Mélange" unit (sample KG-11-36). Phase equilibria diagrams (left) and isopleths of garnet composition (right) for garnet 2a (a), 2b (b) and 2c (c) (see garnet maps in Figure 2 and Figures S1 and S2). The local major element chemical composition was estimated using Xmaptool software based on the large map Figure S1, see analytical procedures and references in Appendix S1), except for the water content recalculated locally for each garnet domain. The black star represents the *P–T* conditions of the best fit between modelled garnet compositions and measured ones. The three phase diagrams are in agreement with similar *P–T* conditions, of 25 ± 2 kbar and 510 ± 20°C, in the temperature domain obtained by the Zr-in-rutile thermometer (Loury et al., 2015)

3.2.3 | Mineral compositions

When present, garnet is almandine rich ($Alm_{60\text{-}64}$–$Grs_{22\text{-}28}$–$Sps_{0.05\text{-}0.15}$–$Prp_{02\text{-}04}$; Table S8). There is no clear growth compositional zoning. White mica compositions for all HPMU samples are presented in Table S9 and Figure 7. White mica has a phengitic composition with Si ≥3.19 atoms per formula unit (apfu) and X_{Na} [=Na/(Na+K+Ca)] ≤0.08. Phengite shows compositional variations along the muscovite–celadonite trend with a pyrophyllite content systematically <10% (Figure 7). Phengite Si value ranges (from west to east) from 3.33 to 3.51 apfu in the Tash-Rabat valley (KG-11-43, KG-14-55), 3.30 to 3.44 apfu in the Orto-Keltebek valley (KG-12-64), 3.31 to 3.42 apfu in the Ak-talaa valley (KG-12-50) and 3.19 to 3.44 apfu in the Bash-Qaïyndy valley (KG-12-74). No correlation of Si values with X_{Na} is observed except for samples KG-11-43 and KG-14-55, both from the Tash-Rabat valley, which suggests variable Si^{4+} variations at fixed Na reflecting some isothermal decompression. In contrast, samples KG-11-43 and KG-14-55 show a negative correlation suggesting that these latter are affected by an increase of the vacancies on the A-site which is linked to the alteration of phengite into clay during retrogression (e.g., fig. 4 in Lanari et al., 2013).

Chlorite has an intermediate composition between daphnite (0.34–0.36), clinochlore (0.35) and amesite (0.24–0.25) end-members with a lower sudoite content (0.03–0.07; Table S10). Al^{IV} comprises between 1.20 and 1.28 apfu and X_{Mg} [=Mg/(Mg+Fe)] is of 0.50 ± 0.01.

3.2.4 | Thermobarometry

Figure S3 shows the characteristic Raman spectra of carbonaceous material (see Appendix S1 for the methodology). Extraction of key spectral signatures indicates maximum temperatures (T_{max}) of ~545 ± 50°C in the Tash-Rabat valley, ~560 ± 50°C in the Orto-Keltebek valley, ~565 ± 50°C in the Ak-Talaa valley and ~570 ± 50°C in the Bash-Qaïyndy valley (Figure 8; Table S14). These results suggest a relatively homogeneous T_{max} throughout the Atbashi Range as some previous works showed that RSCM thermometry can detect inter-sample relative variations as small as 10–15°C (Beyssac, Bollinger, Avouac, & Goffé, 2004).

For each sample, the mica–quartz–water equilibrium curves suggest pressure conditions variations higher than the relative uncertainty (Figure 8) reflecting the natural phengite compositional variability observed in each sample (Figure 7). The T_{max} obtained by Raman spectroscopy were used to retrieve the maximum pressure conditions of phengite crystallization, assuming that phengite most likely re-equilibrated at the maximum temperature reached by the sample. This is supported by the Si values of phengite, which agree for a post-P_{max} equilibrium of the phengite in our context. The relative temperature uncertainty on the T_{max} (2σ) was combined

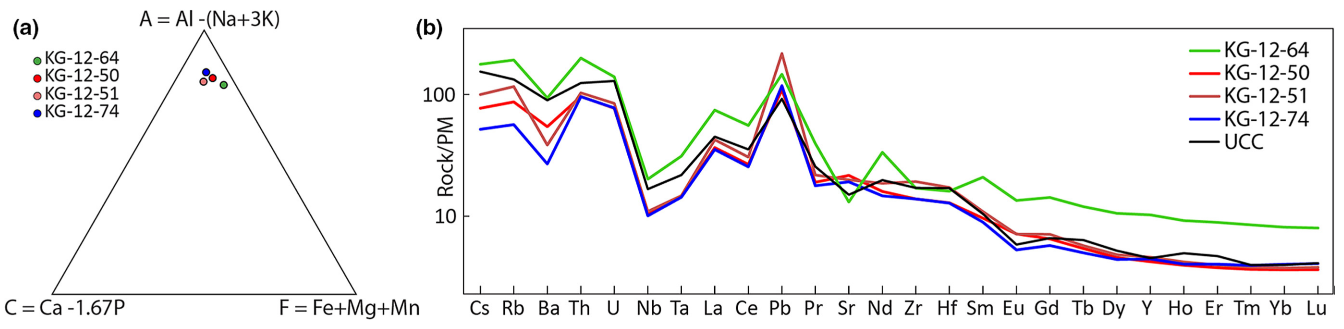

FIGURE 4 (a) ACF diagram showing the aluminous composition of samples of the HPMU suggesting a metapelitic protolith. (b) Primitive mantle normalized trace elements compositions of the HPMU metasedimentary rocks compared with the average Upper Continental Crust (UCC) composition of Rudnick and Gao (2003)

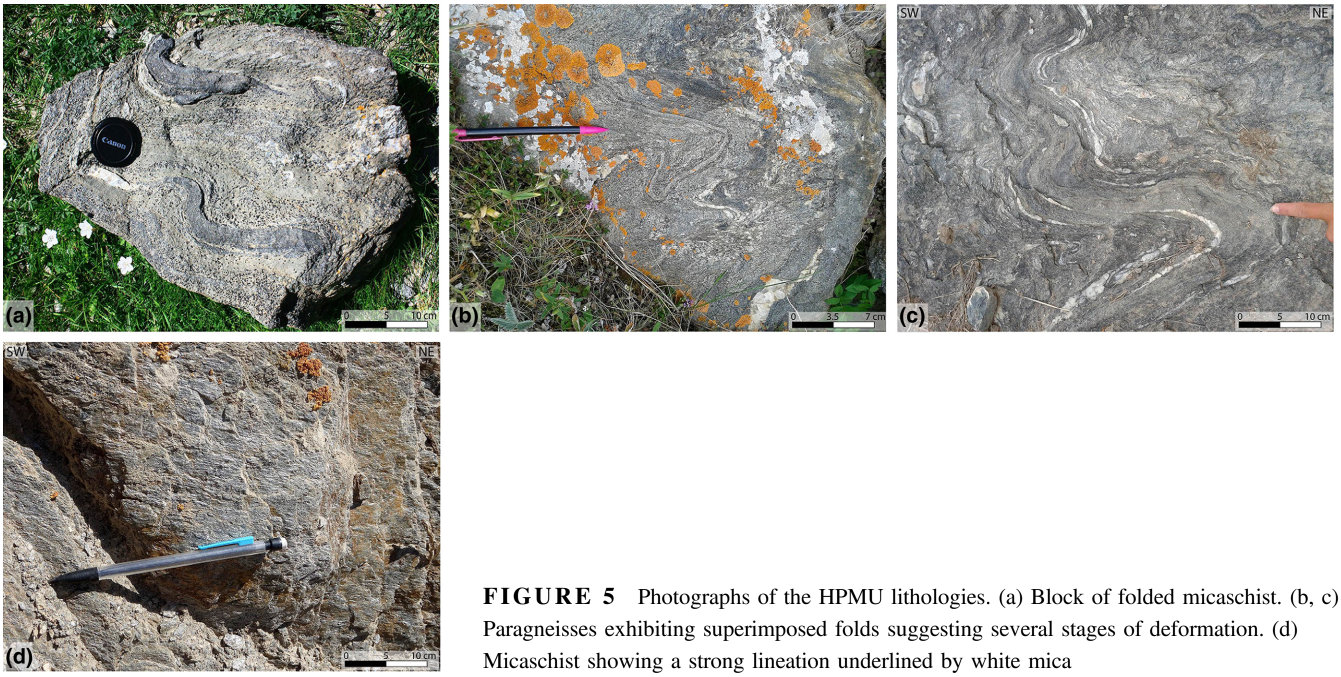

FIGURE 5 Photographs of the HPMU lithologies. (a) Block of folded micaschist. (b, c) Paragneisses exhibiting superimposed folds suggesting several stages of deformation. (d) Micaschist showing a strong lineation underlined by white mica

together with the pressure variability of each sample to approximate the minimum uncertainty on pressure. Sample KG-12-64, from Orto-Keltebek Valley, yields a pressure of 22.9 ± 1 kbar for a T_{max} of ~560 ± 50°C. For Ak-Talaa Valley, T_{max} and phengite equilibria were determined on two different samples, collected at the same outcrop. Sample KG-12-50 indicates a pressure of 20.0 ± 1.2 kbar for ~565 ± 50°C (T_{max} determined on sample KG-12-51). Sample KG-12-74 from Bach-Qaïyndy Valley records a pressure of 23.5 ± 0.5 kbar for a T_{max} of ~570 ± 50°C. Samples KG-11-43 and KG-14-55, from the Tash-Rabat valley, return higher pressure conditions for phengite, ~25–28 kbar at a temperature of 545 ± 50°C.

Chlorite–quartz–water thermometry was applied on the sample KG-12-64 following the method of Vidal, Parra, and Vieillard (2005) and Vidal et al. (2006). The XFe^{3+} varies between 0.18 and 0.33 at 5 kbar and between 0.21 and 0.32 at 10 kbar. Temperature estimates of chlorite are between 275 and 360°C at 5 kbar and between 290 and 340°C at 10 kbar (Figure 9a).

In order to confirm these results, isochemical phase equilibria diagrams were calculated for a sample of the Orto-Keltebek valley (KG-12-64) (Figure 10). Phengite Si value and X_{Mg} ratio isopleths were calculated. Intersection of the highest Si isopleth (3.44 apfu) with corresponding X_{Mg} (0.68) and V(A) (0.06) indicates *P–T* conditions of 560 ± 25°C and 25 ± 2 kbar. These *P–T* conditions are slightly higher than those of Loury et al. (2015) on the same unit, which is ascribed to the application of the more appropriate calibration of Holland and Powell (1998) in the present study. The corresponding mineral assemblage is garnet, phengite, amphibole, clinopyroxene, chloritoid, rutile and lawsonite. Textural evidence is in line with pseudomorphic replacement of lawsonite and jadeite. The presence of albite and titanite together with the absence of paragonite constrains a narrow *P–T* field for retrograde conditions between 300 and 400°C and pressure <6.5 kbar. Combined with the formation temperature derived from chlorite, this *P–T* field can be refined to 300–360°C and 5–6 kbar.

3.2.5 | $^{40}Ar/^{39}Ar$ dating

Analytical procedures for the $^{40}Ar/^{39}Ar$ dating method are displayed in Appendix S1. Phengite from four samples of the HPMU were dated, from the Tash-Rabat (KG-14-52, KG-14-56), Ak-Talaa (KG-12-51) and Bach-Qaïyndy (KG-12-74) valleys. Figure 11 presents the age spectra, and Table S16 displays the data.

KG-14-52

Three duplicates were analysed (Figure 11a). The grain 02 shows strongly decreasing apparent ages in the low-*T* part of the spectrum. For the higher temperature part, a plateau age is defined, at 339.8 ± 3.7 Ma (MSWD = 1.93) corresponding to 69% of ^{39}Ar released in seven steps. The grain 04 shows a slight U-shape spectrum and gives a plateau age of 320.5 ± 3.7 Ma (MSWD = 1.63) corresponding to 99.4% of ^{39}Ar released in 10 steps. The grain Mp also shows decreasing apparent ages in the low-*T* part of the spectrum. For the higher temperature part, a "pseudo-plateau" is obtained at 316.9 ± 2.5 Ma (MSWD = 0.79) corresponding to 55% of

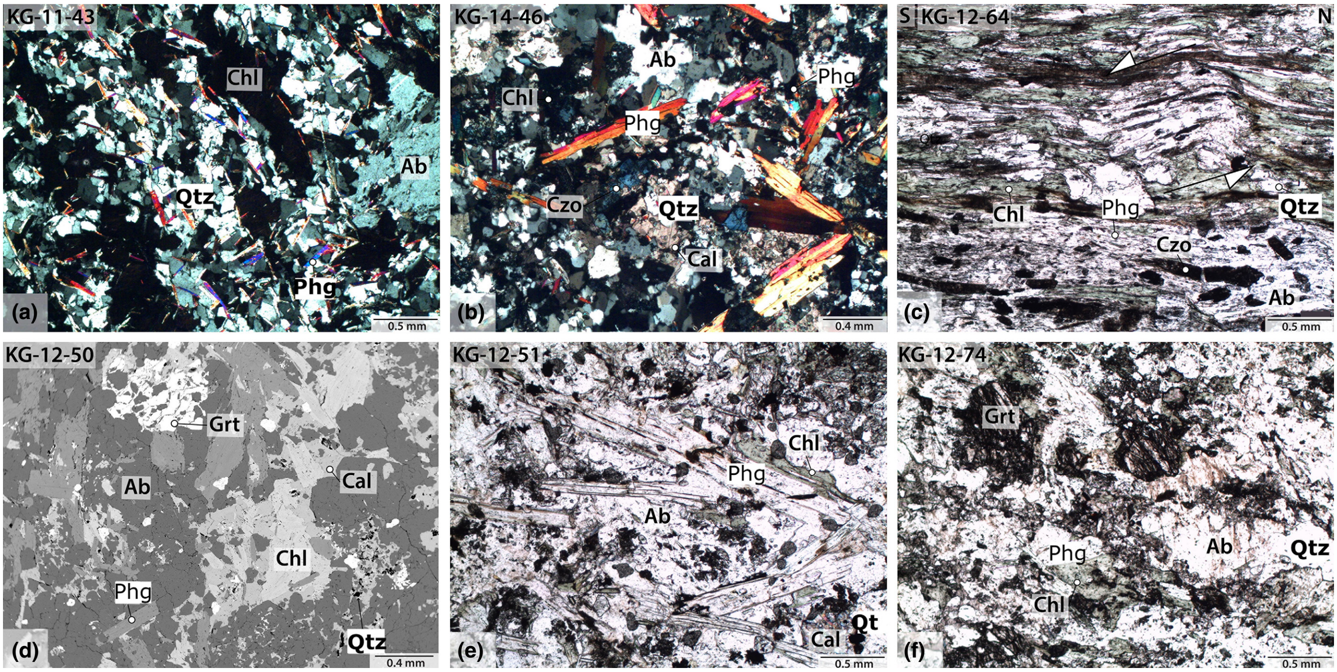

FIGURE 6 Photomicrographs of samples from the HPMU showing various degrees of retrogression in the greenschist facies: (a) Quartzite (KG-11-43) of the Tash-Rabat valley showing a weak foliation marked by chlorite (crossed-polarized light); (b) Micaschist (KG-14-46) of the Tash-Rabat valley (crossed-polarized light); (c) Micaschist (KG-12-64) of the Orto-Keltebek valley showing secondary albite replacing lawsonite (plane-polarized light); (d) Back-scattering electron (BSE) image of paragneiss (KG-12-50) of the Ak-Talaa valley showing a relict garnet; (e) Paragneiss (KG-12-51) of the Ak-Talaa valley showing millimetre-size phengite (plane-polarized light); (f) Paragneiss (KG-12-74) of the Bash Qaïyndy valley, showing relicts of garnet (plane-polarized light) and albite pseudomorphs of lawsonite

^{39}Ar released in five steps. These spectra shapes suggest the presence of excess argon in the analysed grains, and thus, the ages are interpreted as maximum ages.

KG-14-46

One phengite grain was analysed for this second sample of Tash-Rabat Valley (Figure 11b). A plateau age cannot be calculated for this grain; however, a "pseudo-plateau" age is defined at 325.4 ± 2.7 Ma (MSWD = 2.26) corresponding to 44% of ^{39}Ar released in three steps.

KG-12-51

Two phengite grains were analysed (Figure 11c). For the grain 02, a pseudo-plateau age is defined at 322.8 ± 3.0 Ma (MSWD = 4.59) corresponding to 87% of ^{39}Ar released in seven steps. The grain Mp gives a plateau age of 319.1 ± 2.5 Ma (MSWD = 0.09) corresponding to 85% of ^{39}Ar released in four steps.

KG-12-74

Three duplicates were analysed (Figure 11d). The three grains give plateau ages of 324.3 ± 3.2 Ma (MSWD = 0.33), 322.6 ± 3.2 Ma (MSWD = 0.97) and 328.3 ± 2.5 Ma (MSWD = 0.36) corresponding to 97, 100 and 98% of ^{39}Ar released in 8, 12 and 6 steps, respectively. Isochron ages were calculated for this sample (Figure 11e). The grain 01 yields an isochron age of 322.8 ± 3.2 Ma (MSWD = 1.02), consistent within errors with the plateau age. The corresponding ^{40}Ar/^{36}Ar intercept is at 298.8 ± 7.1, which is similar to the atmospheric argon value (Mark, Stuart, & de Podesta, 2011). It follows that the trapped argon is atmospheric and that there is no excess argon in this grain. Similarly, the grain 03 and Mp yield isochron ages of 322.7 ± 3.3 Ma (MSWD = 1.05) and 329.3 ± 2.7 Ma (MSWD = 4.62), respectively, consistent with the plateau ages of these grains. The corresponding ^{40}Ar/^{36}Ar intercepts are at 294.7 ± 25.9 and 299.5 ± 12.5, respectively, which also suggests no excess argon in these grains.

3.3 | Accretionary prism

3.3.1 | Metabasite geochemistry

Metabasites of the Tash-Rabat Valley have low SiO_2 (46–49 wt%) and are alkaline, with Na_2O+K_2O between 4.2 and 5.7 wt%. The X_{Fe} [Fe/(Fe+Mg)] ratios are between 0.64 and 0.70. Metabasites are enriched in LREEs compared with HREEs, with a $(La/Lu)_N$ ratio between 45 and 52 (Figure 12a). They have an intermediate composition between

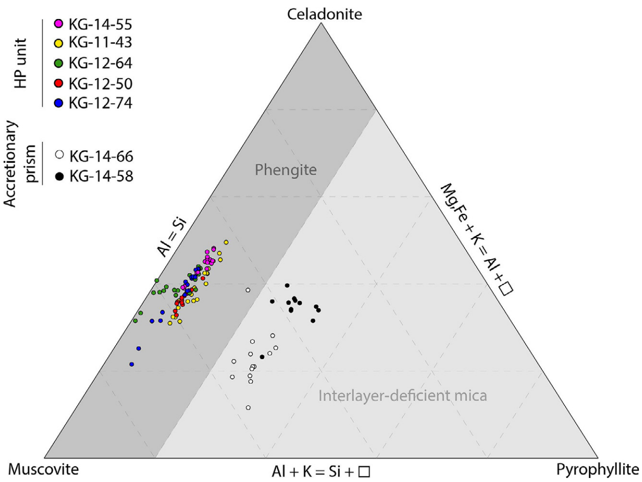

FIGURE 7 Triangular diagram showing the composition of white mica from the HPMU (coloured circles) and from the accretionary prism (black and white circles)

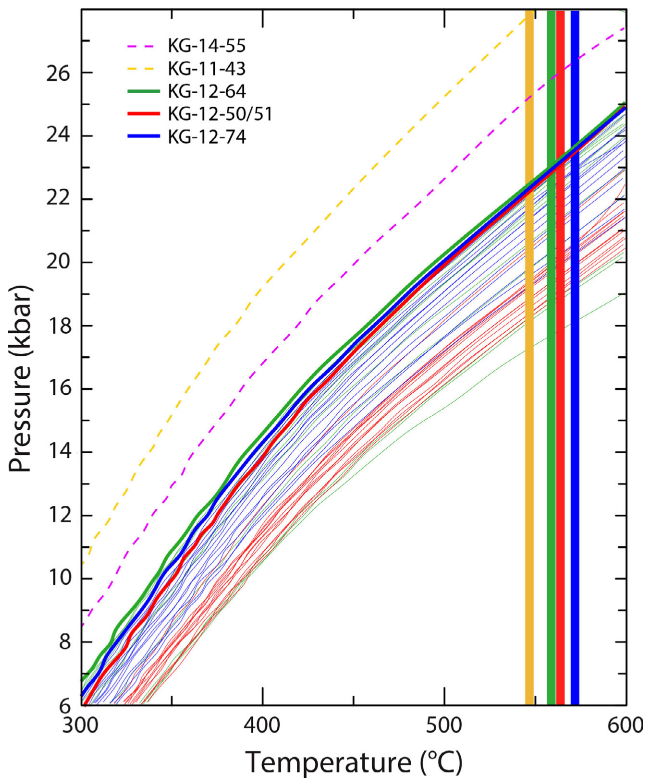

FIGURE 8 *P–T* diagram showing the location of phengite equilibria (Dubacq, Vidal, & de Andrade, 2010) for (a) the HPMU samples. The corresponding maximal temperature (T_{max}) obtained by RSCM is shown by a bold line. Dashed lines represent phengite equilibria that cannot be combined with T_{max} to constrain pressure conditions because of retrogression

enriched-MORB (E-MORB) and OIB. There is no Nb–Ta negative anomaly with Nb/La ratio between 1.07 and 1.19, suggesting the absence of any subduction component. Their $(La/Sm)_N$ ratio, sensitive to mantle source characteristics, comprises between 1.73 and 2.31, similar to typical OIB and seamounts (John, Schenk, Haase, Scherer, & Tembo, 2003; Figure 12b). Th/Yb and Nb/Yb ratios, of 0.63–0.84 and 7.13–9.10, respectively, are between typical E-MORB and OIB within the MORB-OIB array of Pearce (2008; Figure 12c).

3.3.2 | Petrology

Schists

Schists of the Tash-Rabat Valley (samples KG-14-66 and KG-14-58) are fine-grained calcschists with variable amounts of white mica (0–30 vol.%) and chlorite (0–20 vol.%). White mica is interlayer deficient (Figure 7) with low Na+K content, between 0.54 and 0.83 apfu Si value ranges from 3.1 to 3.5 apfu. A negative correlation between Na+K and Si suggests that these high Si values are due to pyrophyllitic substitution. Chlorite has an intermediate composition between amesite, clinochlore, daphnite and sudoite ($Ames_{15-32}$–$Clin_{28-41}$–$Daph_{33-42}$–Sud_{1-12}; Table S10). Al^{IV} value ranges from 0.84 to 1.20 pfu.

Metabasites

In the Tash-Rabat valley, metabasites are associated with metaconglomerates (Figure 13a–c) and slates (Figure 13d), suggesting a volcano-sedimentary origin. Conglomerates contain mafic pebbles, which are sometimes elongated (Figure 13b) in a fine-grained silicic matrix. Pebbles have a fine to very fine-grained texture and contain amphibole+albite±clinopyroxene±epidote ±calcite±quartz±chlorite±titanite assemblage (Figure 14a,b). The matrix is very fine grained and made of an epidote+albite+clinopyroxene+amphibole±titanite assemblage (Figure 14a–c). Conglomerates contain occasionally deformed marble pebbles (Figure 13c).

The slates show a fine bedding with alternations of blueish and greenish beds (Figure 13d). The texture is very fine grained, and the mineral assemblage is similar to the conglomerate matrix with alternations of chlorite+epidote beds with albite+amphibole+chlorite+clinopyroxene±quartz beds (Figure 14d–f).

Clinopyroxene occurs as 0.2–0.5 mm grains, which have an augite composition (Table S13). Amphibole grains are green, blue or have an intermediate colour reflecting a wide range in compositions from alkaline to calcic amphibole (Figure 15; Table S11). Following the classification of Leake (1978), the alkaline amphibole (blue amphibole) has a magnesio-riebeckite composition, the sodic-calcic amphibole has a winchite composition, and the more calcic amphibole (green amphibole) has an actinolite composition. Despite these variations in Na and Ca contents, all the grains have a $(Na+K)_A < 0.5$ pfu and a X_{Mg} ratio between 0.5 and 0.9. Clinopyroxene grains have fractures filled by blue

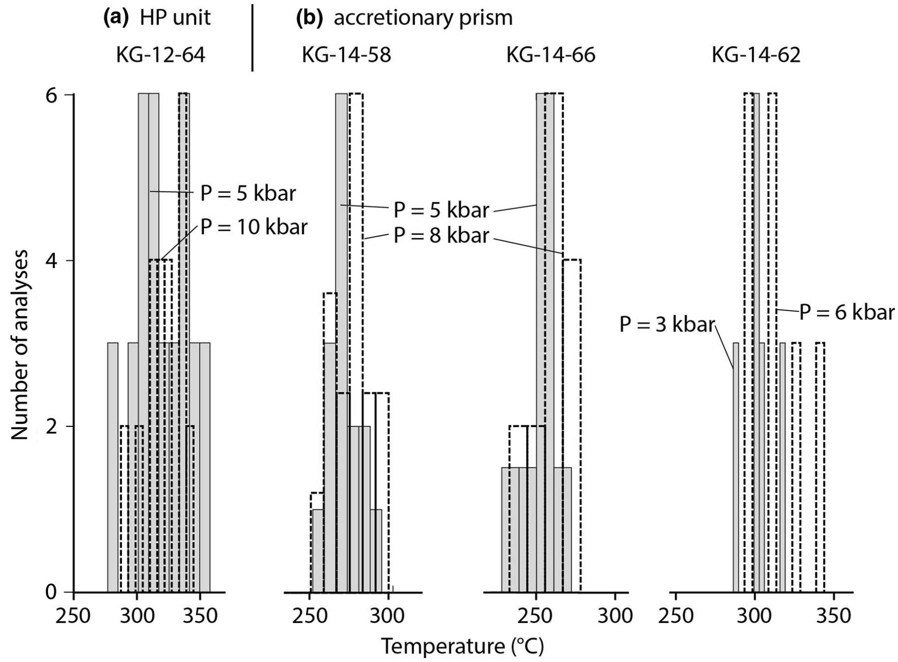

FIGURE 9 Histogram of chlorite temperature obtained with the method of Vidal et al. (2005, 2006) for (a) the HPMU sample KG-12-64 and (b) the accretionary prism samples (calcschist and metabasite)

amphibole and are overgrown by green amphibole. These chemical and textural characteristics of clinopyroxene and amphibole suggest that clinopyroxene is a magmatic relict. Epidote occurs as small grains, 5–10 μm in size and has a composition of Ep_{80}-Czo_{20} (Table S12).

3.3.3 | Thermobarometry

Schists

Maximum temperature recorded by micaschists and calcschists of the accretionary prism has been estimated in a previous study at ~340°C by RSCM (Jourdon, Petit, et al., 2017). In addition, chlorite temperatures were estimated for samples KG-14-58 and KG-14-66, which range between 250–300°C and 230–275°C, respectively (Figure 9b). The pressure change influence on estimated temperatures is <10°C. In chlorite, XFe^{3+} ranges from 0.35 to 0.45 for KG-14-58 and from 0.21 to 0.44 for KG-14-66.

Metabasites

Chlorite–quartz–water thermometry yields temperatures of 285–320°C at 3 kbar and 290–345°C, at 6 kbar (Figure 9b). In addition, an isochemical phase diagram was computed for sample KG-14-62 (Figure 16). The observed paragenesis, at equilibrium, of albite+amphibole+epidote+chlorite+quartz+titanite is modelled at a pressure <5.5 kbar at 275°C and <6.5 kbar at 500°C. This broad *P–T* field can be restrained by combining X_{Ep} isopleths, ranging from 0.74 to 0.90, and temperature obtained from chlorite thermometry. Results indicate that this sample recorded a pressure decrease from 5.5 to <3 kbar at temperature 340–290°C (Figure 16).

4 | DISCUSSION

4.1 | Pressure and temperature conditions

4.1.1 | LP blueschist facies accretionary prism

Metabasites of the accretionary prism in the Tash-Rabat valley recorded peak *P–T* conditions of 5–6 kbar and 290–340°C corresponding to upper greenschist facies conditions, close to the boundary with the blueschist field. Therefore, despite the blue appearance of these rocks, due to Mg-riebeckite (and not to glaucophane), they did not record any typical blueschist facies metamorphic conditions. Calcschists of the same unit recorded consistent T_{max} at ~340°C (Jourdon, Petit, et al., 2017). For metabasites, the epidote compositional range combined with chlorite thermometry suggests a near isothermal decompression to 3 kbar, at 280–320°C. It follows that this unit represents the upper part of the accretionary prism in a similar way as LS Unit of “Schistes Lustrés” in the Alps (e.g., Rolland, Lardeaux, Guillot, & Nicollet, 2000) or Catalina schists in California (Sorensen, 1988).

4.1.2 | HP tectonic mélange

The *P–T* estimates from this unit, based on the zoned pattern of garnets in mafic eclogitic boudins (Figures 2, 3 and 17), are of 510 ± 20°C and 25 ± 2 kbar. They are consistent, though the pressure is slightly higher, with previous *P–T* estimates for the same rocks ranging

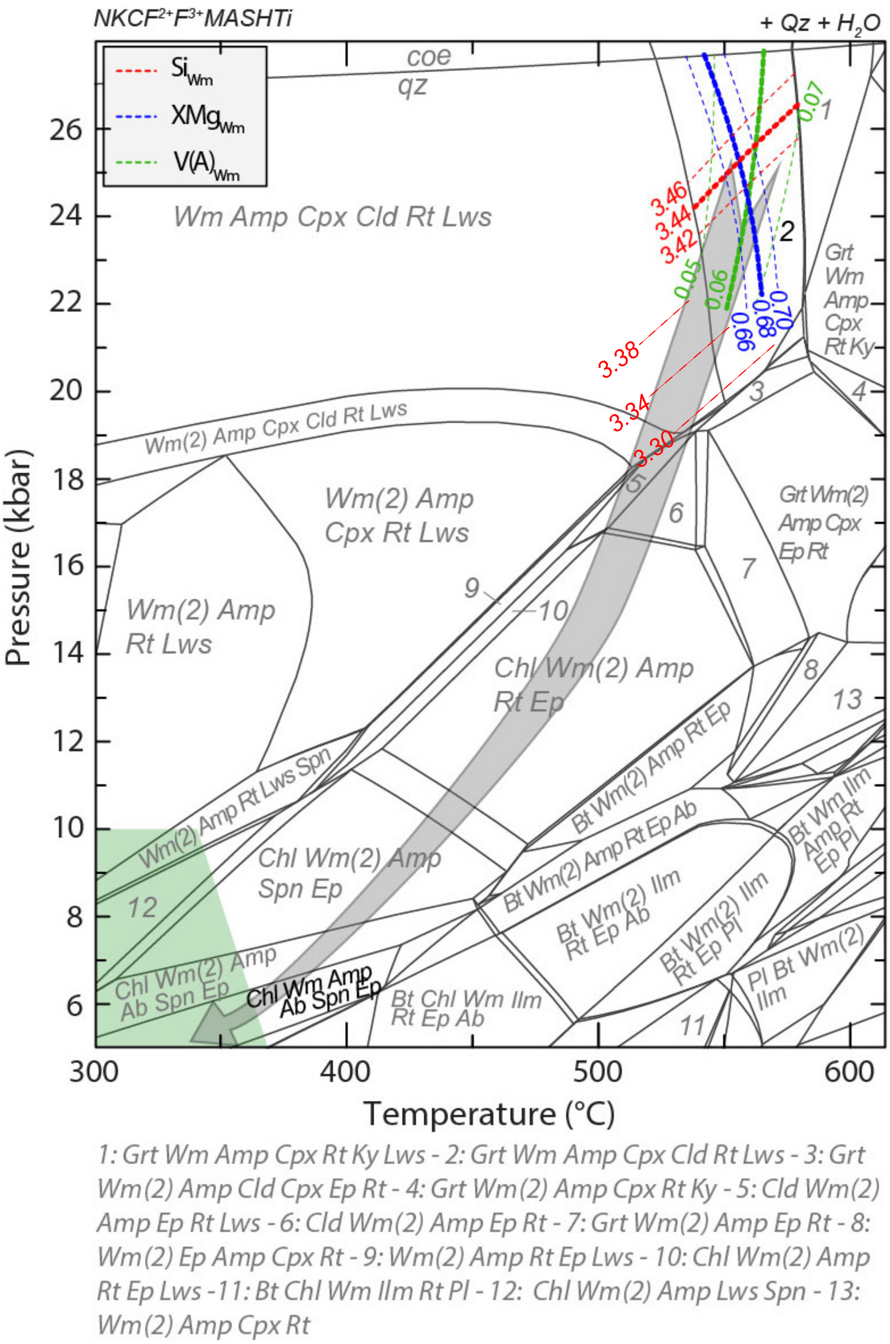

FIGURE 10 *P–T* phase equilibria diagram for sample KG-12-64 (Orto-Keltebek valley) of the HPMU calculated in the NKCFe^{2+}Fe^{3+}MASHTi system. The chemical composition used as input is reported in Table S14. For isopleths, dotted lines represent values for KG-12-64 phengite with the highest Si content. The green field indicates results of chlorite thermometry. The arrow represents the deduced *P–T* path. Mineral abbreviations are after Whitney and Evans (2010) except "Wm" for white mica. Wm(2) indicates that two mica phases are stable (generally phengite and paragonite)

between 510°C–18 kbar and 660°C–25 kbar (Hegner et al., 2010; Loury et al., 2015; Simonov et al., 2008). The temperature estimates are also consistent with a maximum value of 510 ± 25°C obtained from Zr-in-rutile thermometry (Loury et al., 2015). This *P–T* evolution implies a burial along a low geothermal gradient of ~5.6°C/km (Figure 17). A similar gradient is reported for eclogites found in a similar structural position in the Chinese south Tien-Shan range in western China, which recorded *P–T* conditions of 520–540°C and 28–30 kbar (Tian & Wei, 2013) confirming the existence of an east–west along strike continuity of the HP tectonic mélange along the STS range.

4.1.3 | HP metasedimentary unit

Combining RSCM and mica–quartz–water equilibria in the metasedimentary rocks returns homogeneous *P–T* conditions all along the Atbashi range, at 560–570°C and 23–25 kbar. These *P–T* conditions are similar within error to those of mafic eclogites from the Tectonic Mélange unit (Figure 17). The modelled mineral assemblage at these conditions (phengite–amphibole–clinopyroxene–chloritoid–rutile–lawsonite, Figure 10) does not fully match the observations (phengite–albite–quartz–chlorite–epidote–titanite). The observed assemblage is modelled at 300–400°C and <6.5 kbar, which is consistent with chlorite thermometry

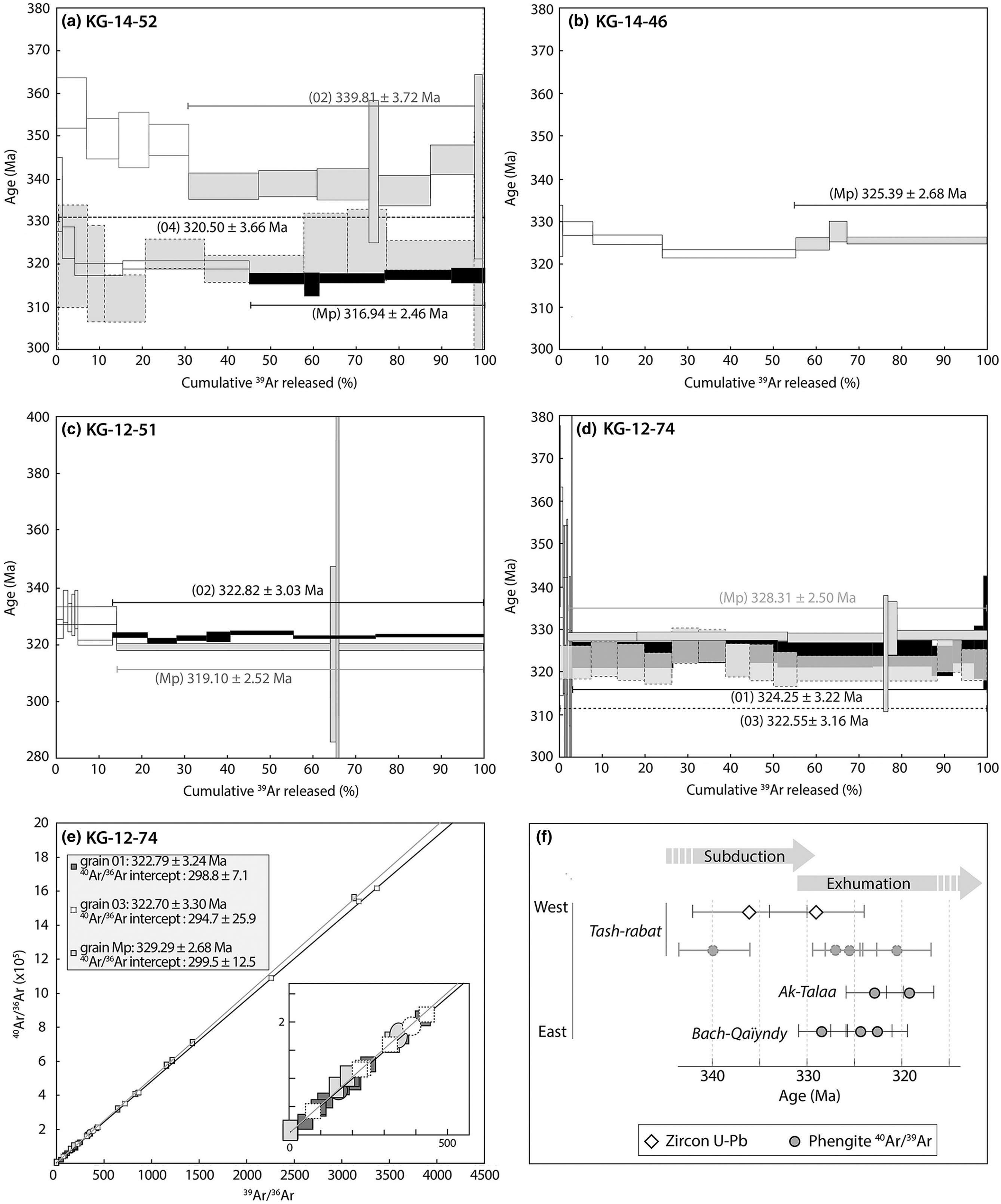

FIGURE 11 $^{40}Ar/^{39}Ar$ step-heating results for the Atbashi Range. (a–d) Age spectra of phengite from the HPMU (see location on Figure 1). Apparent and plateau ages are given at 2σ. Number in parenthesis before the age is for the grain reference for analyses undertaken at Géoazur Nice University, Mp is for grains analysed at Géosciences Montpellier. (e) Isochron plot for sample KG-12-74. Squares represent individual step-heating results and circles correspond to the (bulk) "total fusion" point. (f) Synthesis showing the scattering of plateau ages. Diamonds represent U–Pb on zircon ages obtained by Rojas-Agramonte et al. (2014) on paragneisses from the Tash-Rabat valley

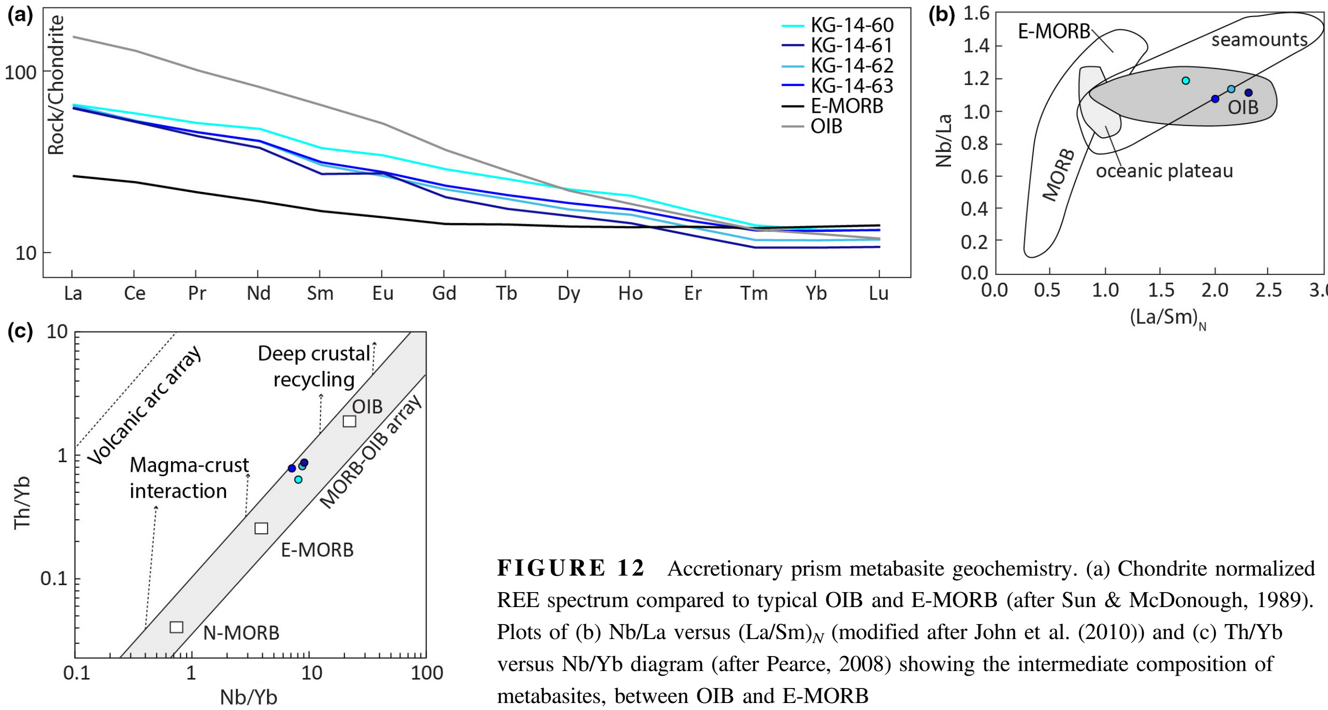

FIGURE 12 Accretionary prism metabasite geochemistry. (a) Chondrite normalized REE spectrum compared to typical OIB and E-MORB (after Sun & McDonough, 1989). Plots of (b) Nb/La versus $(La/Sm)_N$ (modified after John et al. (2010)) and (c) Th/Yb versus Nb/Yb diagram (after Pearce, 2008) showing the intermediate composition of metabasites, between OIB and E-MORB

and thus reflects retrograde *P–T* conditions. Textural evidence for replacement of lawsonite by epidote shows that the assemblage has been transformed during retrogression. However, phengite Si value at these retrograde conditions is predicted to be <3.18 apfu, while analysed phengite has higher Si values 3.33–3.51. This suggests that the phengite interiors are relicts of the HP event and are metastable during the retrogression, and this is relatively common in subduction settings (e.g., Agard, Vidal, & Goffé, 2001; Frey, Hunziker, Jäger, & Stern, 1983). The equilibrium phase diagram in Figure 10 shows that white mica is the only K-bearing stable phase all along the *P–T* path, and thus does not break down to a new phase stable at lower grade conditions. Pressure estimates in these samples are based on phengite compositions. The obtained pressures appear variable (20–25 kbar), as illustrated in Figure 7; phengite exhibits compositional variations along the muscovite–celadonite joint. In all calculations, water activity was fixed at $a_{H_2O} = 1$. Lower water activity values could shift the equilibria towards higher pressures (Massonne & Schreyer, 1987). The influence of reduced a_{H2O} on pressure estimates was tested on mica–quartz–water equilibria (Figure S4). At

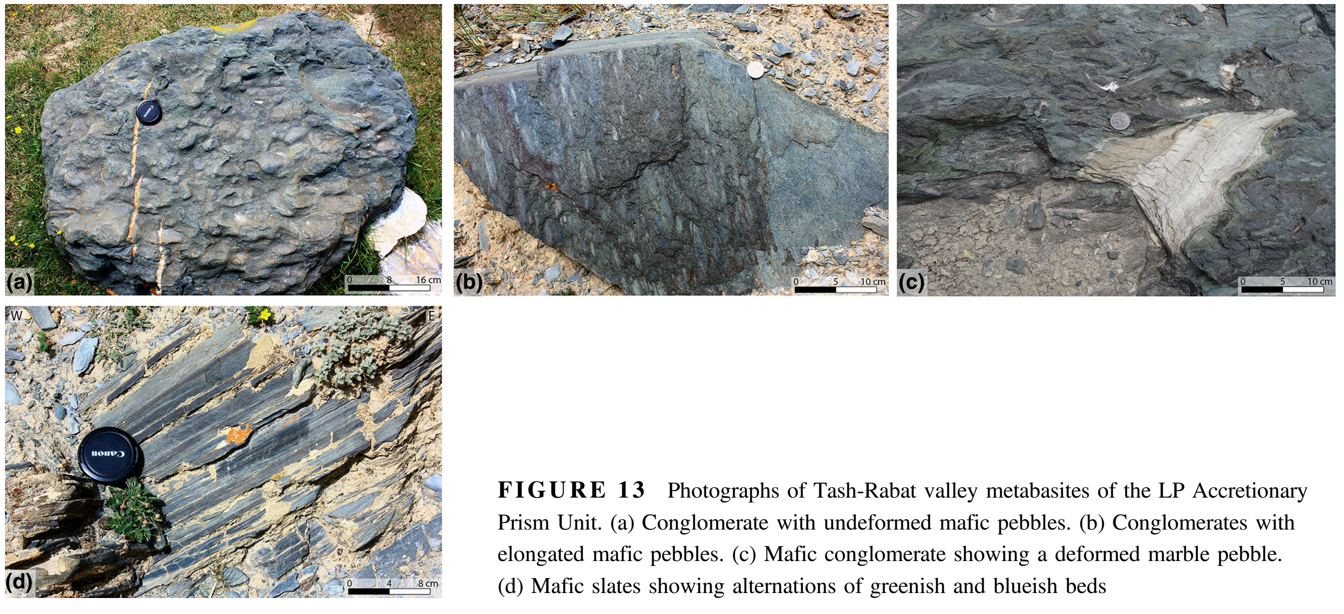

FIGURE 13 Photographs of Tash-Rabat valley metabasites of the LP Accretionary Prism Unit. (a) Conglomerate with undeformed mafic pebbles. (b) Conglomerates with elongated mafic pebbles. (c) Mafic conglomerate showing a deformed marble pebble. (d) Mafic slates showing alternations of greenish and blueish beds

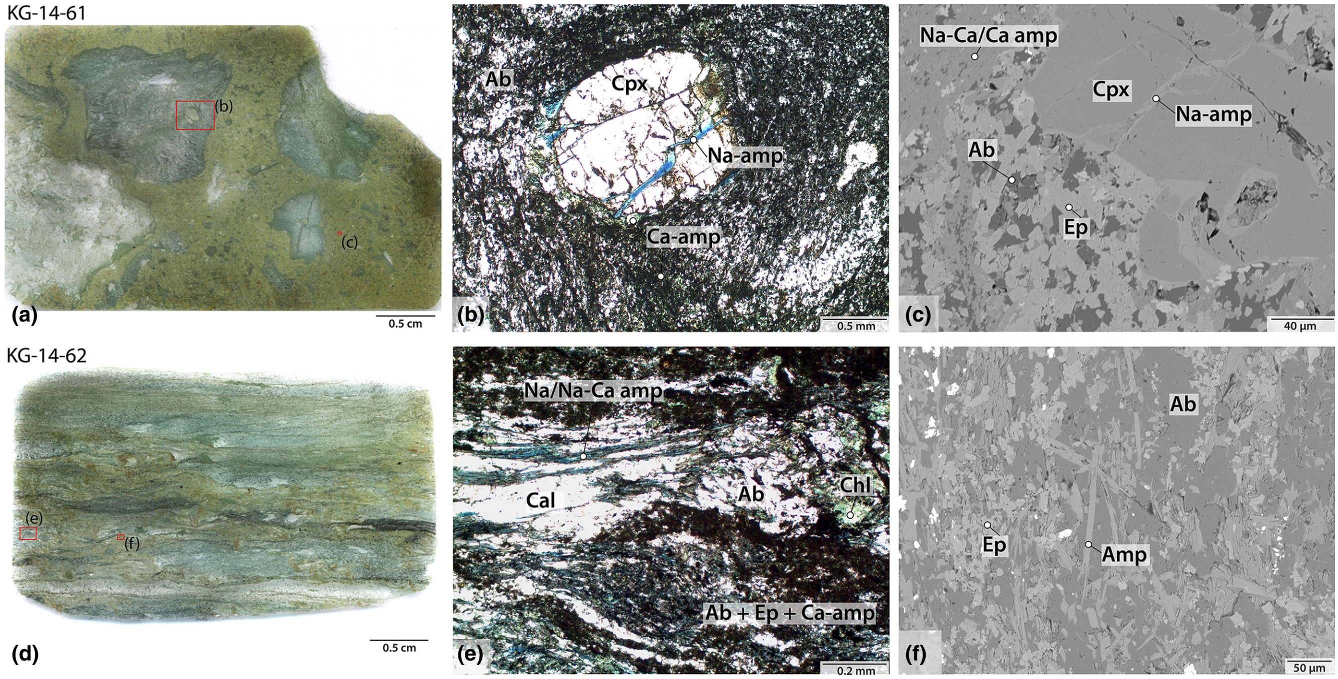

FIGURE 14 Photomicrographs of Tash-Rabat valley metabasites of the LP Accretionary Prism Unit. (a) Thin section photograph of a conglomerate (sample KG-14-61) showing deformed mafic pebbles (pluri-millimetre in size). Red boxes indicate location of (b) and (c). (b) Clinopyroxene in a mafic pebble showing fractures filled by blue amphibole while the outer rim is sealed by green amphibole in a fine-grained matrix. (c) BSE image showing the very fine-grained texture of the matrix (plane-polarized light). A clinopyroxene grain shows fractures filled by Na-amphibole. (d) Thin section photograph of a slate (sample KG-14-62) showing alternations of blueish and greenish beds. Red boxes indicate locations of (e) and (f). (e) Alternations of blueish amphibole+calcite beds with albite+epidote+green amphibole beds (plane-polarized light). (f) BSE image of a greenish bed showing a very fine-grained texture made of epidote+albite+Ca-amphibole

the conditions predicted for the T_{max} (550–600°C), reducing a_{H_2O} to 0.8 induces a pressure increase of 0.5 kbar and lowering a_{H_2O} from 1 to 0.6 induces a pressure increase of 1.3 kbar. The effect of lower a_{H2O} is, thus, negligible as it is lower than the typical errors on *P–T* estimates (±50°C and 2.5 kbar; e.g., Lanari et al., 2013), but could explain the slight variations of phengite Si values observed within and between analysed samples. This feature supports the conclusions drawn in this study, that is, the slightly variable phengite Si values reflect partial re-equilibration during early stages of retrogression (at T_{max} conditions) and the absence of net transfer reactions may explain why phengite is the best relict of HP condition in these samples.

Sang et al. (2017) proposed that the so-called HPMU unit is indistinguishable from the HP tectonic mélange, considering that the HPMU unit consists of blocks of eclogites embedded in a lower grade metasedimentary matrix. By this study, we clearly demonstrate that while the HPMU unit bears a distinct lithology with respect to the HP tectonic Mélange, it also preserves HP assemblages, suggesting that all the lithologies (metasedimentary and metamafic rocks) record HP eclogitic conditions. We, thus, propose that the HP Tectonic mélange and the HPMU are two distinct units and that they both record HP conditions.

4.2 | ^{40}Ar/^{39}Ar dating of phengite and significance for HPMU metamorphic peak and exhumation

^{40}Ar/^{39}Ar ages of phengite from the HPMU range between 339 and 317 Ma. Rojas-Agramonte et al. (2014) obtained similar U–Pb ages of 329 ± 5 and 336 ± 6 Ma on metamorphic overgrowths of detrital zircon from paragneisses of the Tash-Rabat valley, suggesting that the metamorphic peak occurred in this time range (Figure 11f). However, ^{40}Ar/^{39}Ar dating provided a range of significantly distinct ages, out of the error margins. These variations in ^{40}Ar/^{39}Ar age are not ascribed to excess argon as inverse isochron ages show ^{40}Ar/^{36}Ar intercepts with normal air values (Figure 11e). Further, these variations are unrelated to the structural location, as similar ages have been obtained at the HPMU scale (>60 km along strike), while different ages were obtained in a given sample (KG-14-52). Thus, the age variation does not reflect any difference in the timing of uplift and cooling of the HPMU, but is

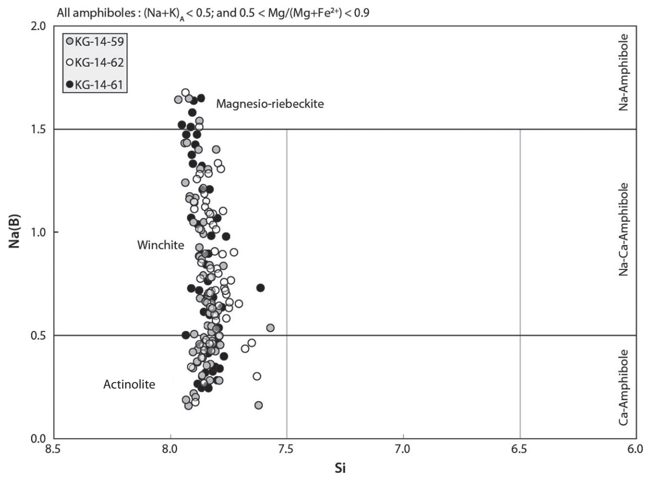

FIGURE 15 Na(B) versus Si diagram illustrating the gradual compositional range from Na- to Ca-amphibole in the metabasites (classification after Leake, 1978)

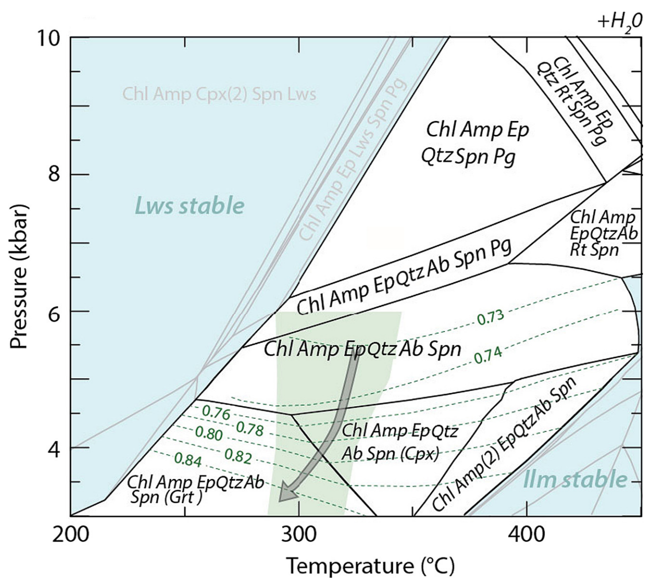

FIGURE 16 P–T phase equilibria diagram for the metabasite sample KG-14-62 calculated in the NKCFe^{2+}Fe^{3+}MASHTi system. Chemical composition used as input is reported in Table S14. The green field indicate results of chlorite thermometry. Green dashed lines are the X_{Ep} isopleths. For clarity, blue area identifies fields where lawsonite or ilmenite are stable, and thus which do not correspond to the observed assemblage. The arrow represents the deduced P–T path. Mineral abbreviation after Whitney and Evans (2010)

ascribed to several crystallization phases or to a recrystallization process (e.g., Airaghi, Lanari, de Sigoyer, & Guillot, 2017; Allaz, Engi, Berger, & Villa, 2011; Sanchez et al., 2011; Villa, 2015). Considering sample KG-14-52, two phengite grains yielded plateau ages of 321 ± 4 Ma and 317 ± 2, similar within errors to those obtained in the other valleys (Figure 11), and one significantly older age of 340 ± 4 Ma. The spectrum of this latter *c*. 340 Ma age (grain 02, Figure 11a) exhibits a complex shape, which might reflect some recrystallization processes. This *c*. 340 Ma age pattern is, thus, in agreement with the partial preservation of a crystallization age from the prograde metamorphic path (e.g., Uunk, Brouwer, ter Voorde, & Wijbrans, 2018; Warren, Hanke, & Kelley, 2012). Apart from this later sample, all ages range from 328 to 319 Ma. We, thus, suggest that plateau age scattering reflects the compositional range of phengite that crystallized or recrystallized in the T_{max} part of the P–T loop, which is almost vertical in the P–T space (e.g., Section 4.1.3). This age span would correspond to the main phase of phengite crystallization, which occurred during a phase of decompression (between 22 and 18 kbar), in agreement with the composition of phengite analysed by EPMA and the corresponding isopleths of Si^{4+}, X_{Mg} and V(A) values on the phase diagrams (see Section 3.2.4, Figure 10). These phengite compositions are those of the T_{max}, which remained at 550°C for *c*. 10 Ma during decompression, and are unlikely to correspond to prograde stages of the P–T path.

4.3 | Significance of the HPMU: Continental crust or deep accretionary prism?

To address the geological significance of HPMU, the obtained $^{40}Ar/^{39}Ar$ ages on the Atbashi HPMU are compared with other key geochronological data from the STS region on Figure 18. The obtained $^{40}Ar/^{39}Ar$ ages are coherent with the obtained ages on the HP metamorphic rocks at the scale of the STS with various techniques (Sm–Nd, U–Pb, Rb–Sr), which mostly range between 330 and 318 Ma. The $^{40}Ar/^{39}Ar$ ages predate by 3–15 Ma the ages ascribed to retrogression during tectonic exhumation of the HP metamorphic units at 315–300 Ma (Du, Zhang, Bader, Chen, & Lü, 2014; Klemd et al., 2005; Figure 18). It follows that the $^{40}Ar/^{39}Ar$ ages likely correspond to phengite crystallization or recrystallization during the onset of exhumation of the Atbashi HPMU.

Further, to reconstruct the full geological history of the HPMU, the question of its original geodynamic context of formation is posed. Protoliths of paragneisses and micaschists constituting the HPMU have a pelitic composition, which is in agreement with the alteration of a granitic continental crust source. In addition, Hegner et al. (2010), Rojas-Agramonte et al. (2014) and Sang et al. (2017) have obtained a protolith age dispersion mainly ranging from 500 to 350 Ma, similar to the North Tien Shan batholiths and clearly distinct from the Tarim craton. It follows that the HPMU metasedimentary rocks likely resulted from the erosion of the North Tien Shan batholiths. Two hypotheses can be proposed for the initial formation of such a pelitic unit: it could either represent (1) the sedimentary cover of

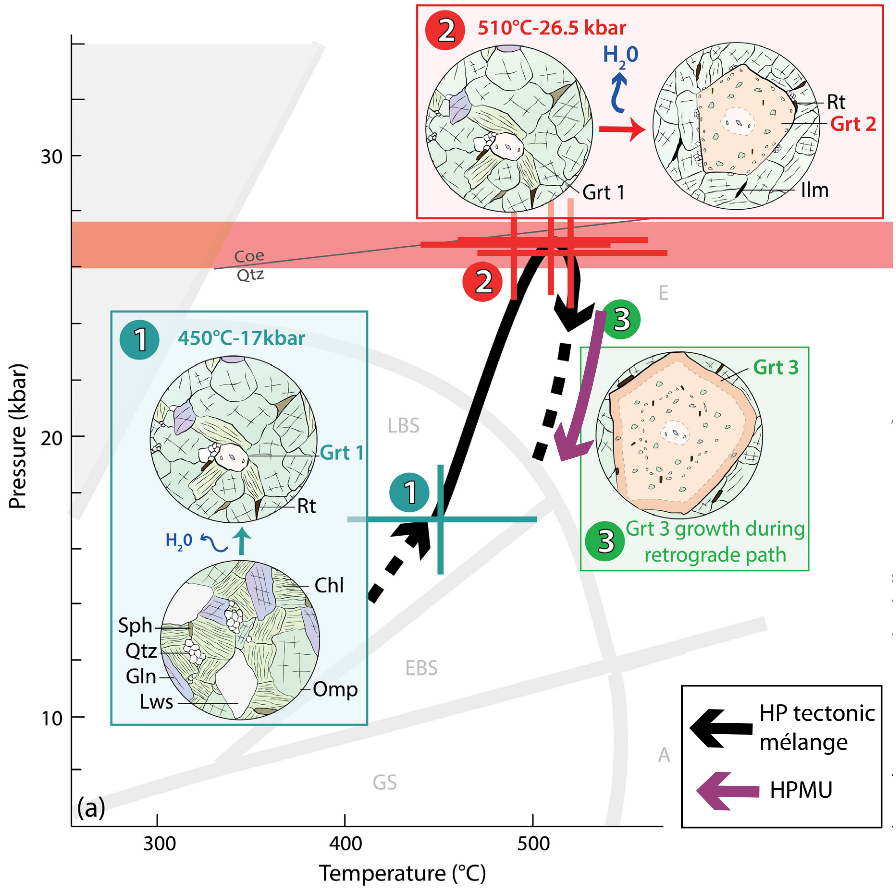

FIGURE 17 Synthetic *P–T* paths of the Tectonic Mélange and HPMU eclogites, and the corresponding evolving texture in the mafic eclogite KG-11-36

a thinned continental margin or (2) the deepest part of the accretionary prism. These two hypotheses have strong geodynamic implications, not only on the HPMU but also on the STS evolution:

1. In the first case (Figure 19a), the HPMU represents the sedimentary cover of the thinned continental margin of MTS (i.e., Kazakhstan microcontinent) originating from the erosion of NTS batholiths. This implies a south-dipping subduction of the Turkestan Ocean under the Tarim craton. At *c.* 320 Ma, after subduction of the thinned continental margin, a decoupling between the continental crust and its sedimentary cover can be proposed. This south-dipping subduction is suggested by the opening of back-arc basins on the northern margin of the Tarim craton between 334 and 309 Ma, and their subsequent closure with top-to-the-North kinematics (Wang et al., 2017).
2. In the second case (Figure 19b), a north-dipping subduction is invoked. In this model, sediment derived from the ongoing erosion of NTS batholiths is incorporated in the accretionary prism. In this case, exhumation occurred during subduction and was driven by the accretionary prism dynamics (e.g., Guillot, Hattori, Agard, Schwartz, & Vidal, 2009). This hypothesis is supported by widespread calc-alkaline magmatism on the Kazakh margin especially in the southern Yili and Central Tien Shan regions in China at 375–328 Ma (Gao et al., 2009; Han et al., 2011; Ma, Shu, Meert, & Li, 2014), though this magmatism was restricted in Kyrgyz MTS (Alekseev et al., 2009). Further, influence of the north-dipping subduction in China is possibly hidden as it coincided with a long-lived south-dipping subduction of North Tien Shan Ocean in Yili—Central Tien Shan since 450 Ma (Han & Zhao, 2017; Ma et al., 2014, Figure 18). Such north-dipping subduction model (2) implies an important thrust system within the accretionary prism to explain the pressure gap between the HPMU and the accretionary prism unit. It also requires a back-thrusting event to obtain the present Atbashi range structure and hardly explains (a) the obduction of unmetamorphosed ophiolite on the MTS and (b) the opening of back-arc basins along the N-Tarim craton margin between 334 and 309 Ma (Wang et al., 2017). Our petrochronological and geological study highlights a large-scale homogeneity of the 125 km long HPMU unit in terms of petrology, *P–T* conditions and exhumation age. In an accretionary prism setting, one would expect heterogeneous *P–T* conditions as, for example, in the “Schistes Lustrés” complex of Western Alps

where P–T conditions evolve continuously during tens of Ma across the unit (Agard, Jolivet, & Goffé, 2001; Rolland et al., 2000; Schwartz, 2000). Moreover, in a palaeo-accretionary prism, it is common to observe oceanic crust remnants represented by mafic blocks of variable sizes in a calc-silicate matrix (Guillot et al., 2009; Tricart & Schwartz, 2006), which is not the case here. Consequently, considering lithological homogeneity of this unit, the similarity of the metamorphic conditions all along the range but also in the different lithologies and the short duration of the HP event (<10 Ma), the hypothesis of a deep accretionary prism origin (Figure 19b) can be discarded. The Atbashi HPMU likely features a large piece of continental crust, derived from the North-Middle Tien Shan passive margin, subducted and exhumed as a whole in the final stages of the Turkestan Ocean subduction and the following collision with the Tarim craton.

3. Therefore, a third scenario could better fit for all observations (Figure 19c). The north-dipping subduction below the MTS would be stopped at *c.* 340–330 Ma, for instance, by an exotic block or an oceanic ridge. This slowing or stopping of the northern subduction would initiate a south-dipping subduction along the northern margin of the Tarim craton. This second subduction would better explain the large-scale south-dipping structure of STS, the relative position of HP units, the opening of back-arc basins and top-to-the-north kinematics.

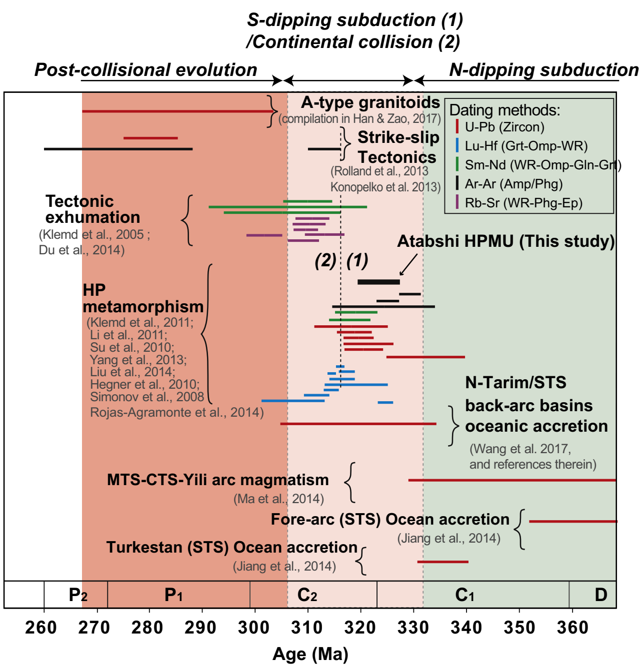

FIGURE 18 Key subduction and collision events in SW Tien Shan. (1) Phase of HP metamorphism, (2) phase of exhumation and retrogression of the HP units

4.4 | Significance of the "HP tectonic mélange"

The lithological features of the HP tectonic mélange are typical of a "subduction channel" (e.g., Angiboust & Agard, 2010). In contrast to the HPMU, the tectonic "HP tectonic mélange" contains mafic eclogite lenses in calc-schist that probably represents the deepest part of the Late Carboniferous accretionary prism (Loury et al., 2015; Sang et al., 2016, 2017). The maximum pressure conditions recorded by this latter unit, that is, 25 ± 2 kbar, and lithological variability (schists, carbonates, mafic boudins derived from MORB), are compatible with a deep subduction channel formed just below the accretionary prism (e.g., Guillot et al., 2009). Thermobarometry shows that this unit likely underwent relatively similar P–T conditions as the HPMU (Figure 17), which may reflect a tectonic juxtaposition of both units at the base of the accretionary prism. The mafic eclogites cropping out in the Ak-Talaa valley are interpreted as palaeo-oceanic crust fragments (Loury et al., 2015) and yield a Sm–Nd age of 319 ± 4 Ma and a similar within error $^{40}Ar/^{39}Ar$ age of 316 ± 3 Ma (Hegner et al., 2010). These ages are similar within error with the younger $^{40}Ar/^{39}Ar$ ages obtained for the HPMU. At the scale of the STS, this age is transitional between the obtained ages for the HP phase (1 in Figure 18) and those of retrogression and LP exhumation (2 in Figure 18). Therefore, the ages recorded by the HP Tectonic Mélange may be interpreted as the crystallization ages of phengite during the deformation phase accommodating the vertical extrusion of HP units within the subduction channel.

4.5 | Tectonic prism dynamics, HP units' exhumation and postcollisional evolution

Following their juxtaposition, extrusion of the HP units was accommodated by a basal thrust with top-to-the-north kinematics at the base of the eclogite facies units (at the base of HP mélange) and by a detachment showing top-to-the-south kinematics to their south (at the top of HPMU; Figure 1; Loury et al., 2015). Therefore, exhumation proceeded in two stages: (a) a phase of deep exhumation occurred while the HPMU was detached from the continental slab and exhumed along the Lithospheric mantle between 25 and 20 kbar (Figure 19). This phase was likely driven by buoyant forces from 70 to 75 km up to 60 km depth, as at these depths, the eclogitized crust is more buoyant than the mantle (Guillot et al., 2009). Following this buoyancy-driven phase, (b) the units were exhumed by tectonic movements within the orogenic prism. Exhumation of HP units was driven by continued

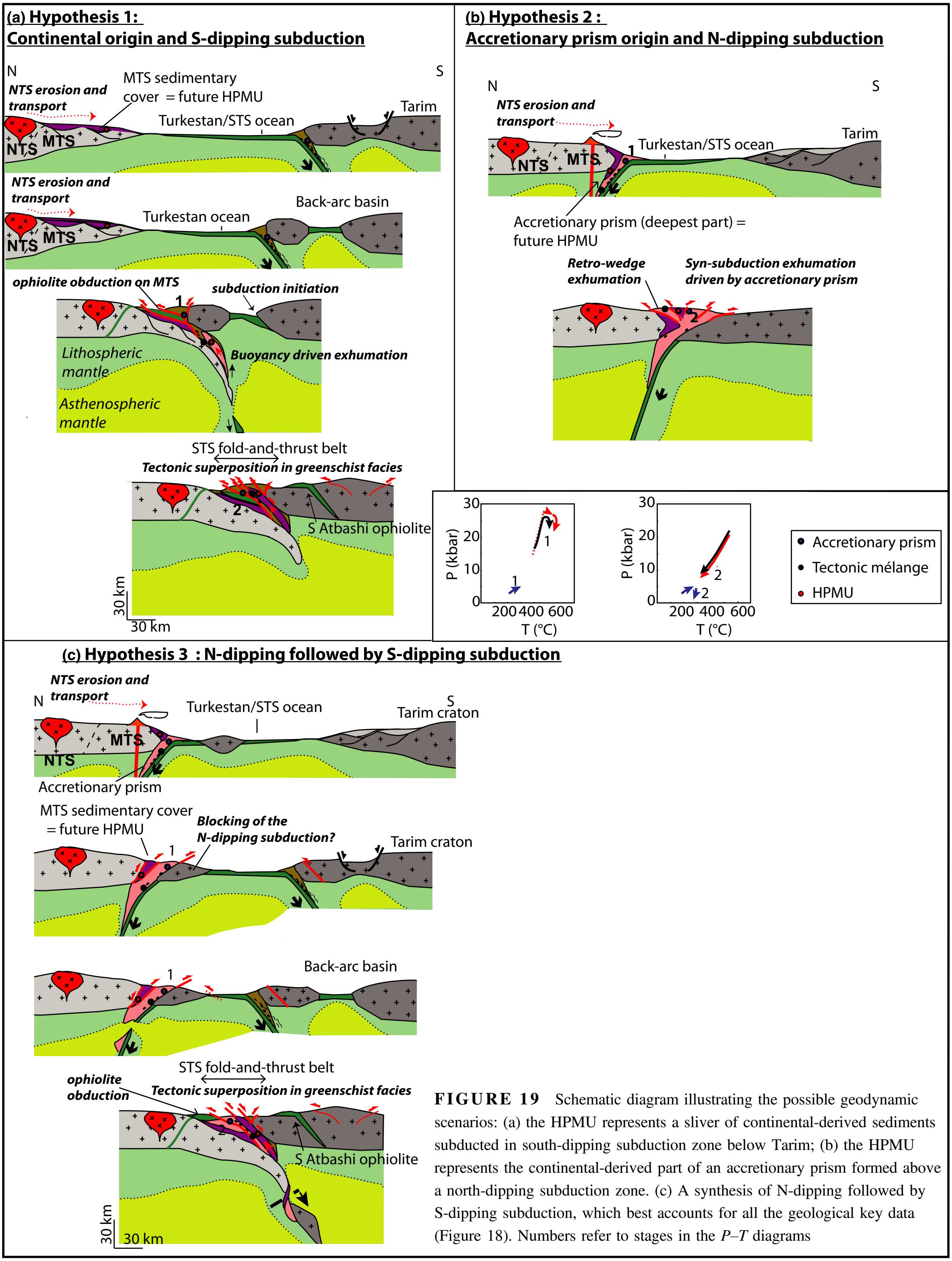

FIGURE 19 Schematic diagram illustrating the possible geodynamic scenarios: (a) the HPMU represents a sliver of continental-derived sediments subducted in south-dipping subduction zone below Tarim; (b) the HPMU represents the continental-derived part of an accretionary prism formed above a north-dipping subduction zone. (c) A synthesis of N-dipping followed by S-dipping subduction, which best accounts for all the geological key data (Figure 18). Numbers refer to stages in the *P*–*T* diagrams

convergence in a collisional style, with propagation of thrusts towards the north as illustrated by the geological cross-section (Figure 1c). The juxtaposition of HPMU with basal prism units accommodated by top-to-the-north shearing occurred at a depth equivalent to a pressure of ~20 kbar. This phase (2 in Figure 19) can be considered as a transition phase from subduction to collision s.s., which commenced at 320–318 Ma with the onset of strike-slip tectonics (Konopelko et al., 2013; Rolland et al., 2013), and ended at 303–295 Ma with the deposition of a posttectonic conglomerate resting unconformably on the high-*P* rocks (Baslakunov, Takasu, Tagiri, Bakirov, & Sakiev, 2007). The postcollisional phase started at *c.* 300 Ma by the onset of widespread A-type magmatism and ongoing strike-slip tectonics in the whole Tien Shan region (Figure 18; see a review in Han & Zhao, 2017).

5 | CONCLUSIONS

This study brings out new constraints on the Atbashi Range metamorphic history, along the STS suture, and permits a better understanding of the end of the Turkestan Ocean closure and the accretion of the Kazakh microcontinent to the Tarim craton. The following points can be emphasized:

1. The HPMU likely represents the sedimentary cover of the thinned continental margin of the Kazakh margin which was subducted southward, under the Tarim craton. This south-dipping subduction stage likely followed a north-dipping subduction stage at 340–330 Ma.
2. The HPMU recorded consistent *P–T* conditions across the range, with a maximum burial at 560–570°C and 23–25 kbar, and thus represents one single, >100 km, slice of continental crust, which was subducted and exhumed as a whole in the STS subduction zone in the Late Carboniferous (peak pressure conditions attained at *c.* 330 Ma).
3. In this context, the 20 Ma age range for $^{40}Ar/^{39}Ar$ ages of phengite (340–319 Ma) is interpreted as reflecting crystallization ages during the prograde to peak metamorphic conditions. Most phengite ages range within 328 and 319 Ma. These ages correspond to the peak thermal conditions (T_{max}) of the *P–T* path, which remained at 500–570°C between 18 and 25 kbar, during early stages of decompression of the HPMU and its tectonic juxtaposition with the eclogitic HP mélange.
4. This age range appears homogeneous for HP metamorphism at the scale of the STS and is, thus, interpreted as the major phase of subduction below the northern margin of the Tarim craton.
5. The eclogitic HP tectonic mélange, which contains mafic eclogite boudins within a metasedimentary matrix, underwent similar *P–T* conditions as the HPMU. These lithologies and conditions most likely represent the deepest part of the subduction channel bounding the base of the accretionary prism.
6. The age of 319–316 Ma obtained for the HP tectonic mélange overlaps with the younger HMPU $^{40}Ar/^{39}Ar$ ages. At the scale of STS, it is transitional with the phase of exhumation of HP units and may mark the onset of HP unit extrusion.
7. The shallower levels of the accretionary prism underwent LP blueschist–HP greenschist facies metamorphism at 290–340°C and 5–6 kbar, which is in agreement with a large pressure gap between the two prism units (17–20 kbar). This pressure gap represents the vertical extrusion of the HPMU and eclogitic HP mélange within the prism, in agreement with the north-bounding thrust and the south-bounding extensional detachment observed on both sides of the eclogite facies units.

ACKNOWLEDGEMENTS

We thank A. V. Mikolaichuk and D. Alexeiev for their expertise and guidance in the field. Field and analytical work were supported by the DARIUS Programme, coordinated by M.F. Brunet and E. Barrier and the DSP-Tibet project founded by the Agence Nationale de la Recherche (ANR-13-BS06-012-01). The French ministry of Research is acknowledged for the first author's PhD grant. We thank V. Magnin for assistance during microprobe analysis and M. Zanti for help during samples preparation. Careful reviews by R. Carosi, by two anonymous reviewers and by the editor-in-chief D. Robinson have significantly helped enhance both formal and scientific aspects of the previously submitted version of this manuscript.

ORCID

Yann Rolland http://orcid.org/0000-0001-9547-6092

REFERENCES

Agard, P., Jolivet, L., & Goffé, B. (2001). Tectonometamorphic evolution of the Schistes Lustres Complex: Implications for the exhumation of HP and UHP rocks in the Western Alps. *Bulletin Société Géologique de France*, *172*, 617–636. https://doi.org/10.2113/172.5.617

Agard, P., Vidal, O., & Goffé, B. (2001). Interlayer and Si content of phengite in HP-LT carpholite-bearing metapelites. *Journal of Metamorphic Geology*, *19*, 479–495. https://doi.org/10.1046/j.0263-4929.2001.00322.x

Airaghi, L., Lanari, P., de Sigoyer, J., & Guillot, S. (2017). Microstructural vs compositional preservation and pseudomorphic replacement of muscovite in deformed metapelites from the Longmen Shan (Sichuan, China). *Lithos*, *282–283*, 262–280. https://doi.org/10.1016/j.lithos.2017.03.013

Alekseev, D. V., Aristov, V. A., & Degtyarev, K. E. (2007). The age and tectonic setting of volcanic and cherty sequences in the ophiolite complex of the Atbashe Ridge (Southern Tien Shan). *Doklady Earth Sciences*, *413*, 380–383. https://doi.org/10.1134/S1028334X07030130

Alekseev, D. V., Degtyarev, K. E., Kotov, A. B., Sal'nikova, E. B., Tret'yakov, A. A., Yakovleva, S. Z, . . . Shatagin, K. N. (2009). Late Paleozoic subductional and collisional igneous complexes in the Naryn segment of the Middle Tien Shan (Kyrgyzstan). *Doklady Earth Sciences*, *427*(1), 760–763. https://doi.org/10.1134/S1028334X09050122

Alexeiev, D. V., Ryazantsev, A. V., Kröner, A., Tretyakov, A. A., Xia, X., & Liu, D. Y. (2011). Geochemical data and zircon ages for rocks in a high-pressure belt of Chu-Yili mountains, southern Kazakhstan: Implications for the earliest stages of accretion in Kazakhstan and the Tianshan. *Journal of Asian Earth Sciences*, *42*, 805–820. https://doi.org/10.1016/j.jseaes.2010.09.004

Allaz, J., Engi, M., Berger, A., & Villa, I. M. (2011). The effects of retrograde reactions and of diffusion on ^{40}Ar–^{39}Ar ages of micas. *Journal of Petrology*, *52*(4), 691–716. https://doi.org/10.1093/petrology/egq100

Allen, M. B., & Vincent, S. J. (1997). Fault reactivation in the Junggar region, northwest China: The role of basement structures during Mesozoic–Cenozoic compression. *Journal of the Geolological Society London*, *154*, 151–155. https://doi.org/10.1144/gsjgs.154.1.0151

Allen, M. B., Windley, B. F., & Zhang, C. (1992). Palaeozoic collisional tectonics and magmatism of the Chinese Tien Shan, central Asia. *Tectonophysics*, *220*, 89–115. https://doi.org/10.1016/0040-1951(93)90225-9

Angiboust, S., & Agard, P. (2010). Initial water budget: The key to detaching large volumes of eclogitized oceanic crust along the subduction channel? *Lithos*, *120*(3), 453–474. https://doi.org/10.1016/j.lithos.2010.09.007

Bakirov, A. B. (1978). *Tectonic position of metamorphic complexes in Tianshan*. Frunze, Russia: Ilim(in Russian).

Bakirov, A. B., & Kotov, V. V. (1988). Eclogite-bearing metamorphic complexes as indicator of the ancient continent collision zone. In Frunze "Ilim", Russia. (Ed.), *Precambrian and lower Paleozoic of Tianshan* (vol. 1052, pp. 4–25). (in Russian).

Bakirov, A. B., & Maksumova, R. A. (2001). Geodynamic evolution of the Tien Shan lithosphere. *Russian Geology and Geophysics*, *42*, 1359–1366.

Baslakunov, J., Takasu, A., Tagiri, M., Bakirov, A., & Sakiev, K. (2007). Two modes of occurrence of eclogites from the Atbashy Range, southern Tien-Shan, Kyrgyzstan. AGU Fall Meeting Abstracts, V41C0730B.

Beyssac, O., Bollinger, L., Avouac, J. P., & Goffé, B. (2004). Thermal metamorphism in the lesser Himalaya of Nepal determined from Raman spectroscopy of carbonaceous material. *Earth and Planetary Science Letters*, *225*, 233–241. https://doi.org/10.1016/j.epsl.2004.05.023

Beyssac, O., Goffé, B., Chopin, C., & Rouzaud, J. N. (2002a). Raman spectra of carbonaceous material in metasediments: A new geothermometer. *Journal of Metamorphic Geology*, *20*, 859–871. https://doi.org/10.1046/j.1525-1314.2002.00408.x

Biske, Y. S. (1995). Late Paleozoic collision of Kirghiz-Kazahkstan and Tarim paleocontinents. *Geotectonics*, *1*, 31–39.

Biske, Y. S., Zubtov, Y. S., & Porshnyakov, G. S. (1985). *Hercynides of the Atbashi-Kokshaal region of the Southern Tian-Shan*. Leningrad, Russia: Leningrad State University (in Russian).

de Capitani, C., & Petrakakis, K. (2010). The computation of equilibrium assemblage diagrams with Theriak/Domino software. *American Mineralogist*, *95*(7), 1006–1016.

Cawood, P. A., Kroner, A., Collins, W.J., Kusky, T.M., Mooney, W.D., & Windley, B.F. (2009). Accretionary orogens through Earth history. In P. A. Cawood & A. Kroner(Eds.), *Earth accretionary systems in space and time*. *Geological Society, London, Special Publications*, *318*, 1–36. https://doi.org/10.1144/sp318.1

Charvet, J., Shu, L., Laurent-Charvet, S., Wang, B., Faure, M., Cluzel, D., . . . De Jong, K. (2011). Palaeozoic tectonic evolution of the Tianshan belt, NW China. *Science China Earth Sciences*, *54*, 166–184. https://doi.org/10.1007/s11430-010-4138-1

Diener, J. F. A., Powell, R., White, R. W. & Holland, T. J. B. (2007). A new thermodynamic model for clino-and orthoamphiboles in the system Na_2O–CaO–FeO–MgO–Al_2O_3–SiO_2–H_2O–O. *Journal of Metamorphic Geology*, *25*(6), 631–656.

Du, J. X., Zhang, L. F., Bader, T., Chen, Z. Y., & Lü, Z. (2014). Metamorphic evolution of relict lawsonite-bearing eclogites from the (U) HP metamorphic belt in the Chinese southwestern Tianshan. *Journal of Metamorphic Geology*, *32*(6), 575–598. https://doi.org/10.1111/jmg.12080

Dubacq, B., Vidal, O., & de Andrade, V. (2010). Dehydration of dioctahedral aluminous phyllosilicates: Thermodynamic modelling and implications for thermobarometric estimates. *Contributions to Mineralogy and Petrology*, *159*, 159–174. https://doi.org/10.1007/s00410-009-0421-6

Engi, M., Lanari, P., & Kohn, M. J. (2017). Significant ages—An introduction to petrochronology. *Reviews in Mineralogy and Geochemistry*, *83*, 1–12.

Ernst, W. G. (1988). Tectonic history of subduction zones inferred from retrograde blueschist P-T paths. *Geology*, *16*, 1081–1084. https://doi.org/10.1130/0091-7613(1988)016<1081:THOSZI>2.3.CO;2

Frey, M., Hunziker, J. C., Jäger, E., & Stern, W. B. (1983). Regional distribution of white K-mica polymorphs and their phengite content in the Central Alps. *Contributions to Mineralogy and Petrology*, *83*, 185–197. https://doi.org/10.1007/BF00373092

Gao, J., & Klemd, R. (2003). Formation of HP–LT rocks and their tectonic implications in the western Tianshan Orogen, NW China: Geochemical and age constraints. *Lithos*, *66*, 1–22. https://doi.org/10.1016/S0024-4937(02)00153-6

Gao, J., Long, L., Klemd, R., Qian, Q., Liu, D., Xiong, X., . . . Yang, F. (2009). Tectonic evolution of the South Tianshan orogen and adjacent regions, NW China: Geochemical and age constraints of granitoid rocks. *International Journal of Earth Sciences*, *98*(6), 1221. https://doi.org/10.1007/s00531-008-0370-8

Giuntoli, F., Lanari, P., & Engi, M. (2018). Deeply subducted continental fragments-Part 1: Fracturing, dissolution-precipitation, and diffusion processes recorded by garnet textures of the central Sesia Zone (western Italian Alps). *Solid Earth*, *9*(1), 167–189. https://doi.org/10.5194/se-9-167-2018

Green, E., Holland, T., & Powell, R. (2007). An order-disorder model for omphacitic pyroxenes in the system jadeite-diopside-hedenbergite-acmite, with applications to eclogitic rocks. *American Mineralogist*, *92*, 1181–1189. https://doi.org/10.2138/am.2007.2401

Guillot, S., Hattori, K., Agard, P., Schwartz, S., & Vidal, O. (2009). Exhumation processes in oceanic and continental subduction contexts: A review. In S. Lallemand & F. Funiciello (eds.), *Subduction zone geodynamics* Frontiers in Earth Sciences (pp. 175–204).

Berlin, Heidelberg: Springer Berlin Heidelberg. https://doi.org/10.1007/978-3-540-87974-9

Han, B. F., He, G. Q., Wang, X. C., & Guo, Z. J. (2011). Late Carboniferous collision between the Tarim and Kazakhstan-Yili terranes in the western segment of the South Tian Shan Orogen, Central Asia, and implications for the Northern Xinjiang, western China. *Earth-Science Reviews*, *109*(3), 74–93. https://doi.org/10.1016/j.earscirev.2011.09.001

Han, Y., & Zhao, G. (2017). Final amalgamation of the Tianshan and Junggar orogenic collage in the southwestern Central Asian Orogenic Belt: Constraints on the closure of the Paleo-Asian Ocean. *Earth-Science Reviews*, In Press. https://doi.org/10.1016/j.earscirev.2017.09.012

Han, Y., Zhao, G., Sun, M., Eizenhöfer, P. R., Hou, W., Zhang, X., . . . Xu, B. (2016). Late Paleozoic subduction and collision processes during the amalgamation of the Central Asian Orogenic Belt along the South Tianshan suture zone. *Lithos*, *246*, 1–12. https://doi.org/10.1016/j.lithos.2015.12.016

Hegner, E., Klemd, R., Kröner, A., Corsini, M., Alexeiev, D. V., Iaccheri, L. M., . . . Windley, B. F. (2010). Mineral ages and P-T conditions of Late Paleozoic high-pressure eclogite and provenance of melange sediments from Atbashi in the south Tianshan orogen of Kyrgyzstan. *American Journal of Science*, *310*, 916–950. https://doi.org/10.2475/09.2010.07

Holland, T. J. B., & Blundy, J. (1994). Non-ideal interactions in calcic amphiboles and their bearing on amphibole-plagioclase thermometry. *Contributions to Mineralogy and Petrology*, *116*, 433–447. https://doi.org/10.1007/BF00310910

Holland, T. J. B., & Powell, R. (1998). An internally consistent thermodynamic data set for phases of petrological interest. *Journal of Metamorphic Geology*, *16*, 309–343.

Holland, T., & Powell, R. (2003). Activity-composition relations for phases in petrological calculations: An asymmetric multicomponent formulation. *Contributions to Mineralogy and Petrology*, *145*, 492–501. https://doi.org/10.1007/s00410-003-0464-z

Jiang, T., Gao, J., Klemd, R., Qian, Q., Zhang, X., Xiong, X. M., . . . Chen, B. X. (2014). Paleozoic ophiolitic mélanges from the South Tianshan Orogen, NW China: Geological, geochemical and geochronological implications for the geodynamic setting. *Tectonophysics*, *612–613*, 106–127. https://doi.org/10.1016/j.tecto.2013.11.038

John, T., Schenk, V., Haase, K., Scherer, E., & Tembo, F. (2003). Evidence for a Neoproterozoic ocean in south-central Africa from mid-oceanic-ridge – Type geochemical signatures and pressure-temperature estimates of Zambian eclogites. *Geology*, *31*, 243–246. https://doi.org/10.1130/0091-7613(2003) 031<0243

John, T., Scherer, E. E., Schenk, V., Herms, P., Halama, R., & Garbe-Schönberg, D. (2010). Subducted seamounts in an eclogite-facies ophiolite sequence: The Andean Raspas Complex, SW Ecuador. *Contributions to Mineralogy and Petrology*, *159*, 265–284. https://doi.org/10.1007/s00410-009-0427-0

Jolivet, M., Dominguez, S., Charreau, J., Chen, Y., Li, Y., & Wang, Q. (2010). Mesozoic and Cenozoic tectonic history of the central Chinese Tian Shan: Reactivated tectonic structures and active deformation. *Tectonics*, *29*, 1–30. https://doi.org/10.1029/2010TC002712

Jourdon, A., Le Pourhiet, L., Petit, C., & Rolland, Y. (2017). The deep structure of Kyrgyz Tien Shan: Modelling the past to better constrain the present. *Tectonophysics*, In Press. https://doi.org/10.1016/j.tecto.2017.07.019

Jourdon, A., Petit, C., Rolland, Y., Loury, C., Bellahsen, N., Guillot, S., . . . Ganino, C. (2017). New structural data on Late Paleozoic tectonics in the Kyrgyz Tien Shan (Central Asian Orogenic Belt). *Gondwana Research*, *46*, 57–78. https://doi.org/10.1016/j.gr.2017.03.004

Klemd, R., Bröcker, M., Hacker, B. R., Gao, J., Gans, P., & Wemmer, K. (2005). New age constraints on the metamorphic evolution of the high-pressure/low-temperature belt in the Western Tianshan Mountains, NW China. *Journal of Geology*, *113*, 157–168. https://doi.org/10.1086/427666

Klemd, R., John, T., Scherer, E. E., Rondenay, S., & Gao, J. (2011). Changes in dip of subducted slabs at depth: Petrological and geochronological evidence from HP-UHP rocks (Tianshan, NW-China). *Earth and Planetary Science Letters*, *310*, 9–20. https://doi.org/10.1016/j.epsl.2011.07.022

Konopelko, D., Seltmann, R., Apayarov, F., Belousova, E., Izokh, A., & Lepekhina, E. (2013). U-Pb–Hf zircon study of two mylonitic granite complexes in the Talas-Fergana fault zone, Kyrgyzstan, and Ar–Ar age of deformations along the fault. *Journal of Asian Earth Sciences*, *73*, 334–346. https://doi.org/10.1016/j.jseaes.2013.04.046

Konopelko, D., Seltmann, R., Biske, G., Lepekhina, E., & Sergeev, S. (2009). Possible source dichotomy of contemporaneous post-collisional barren I-type versus tin-bearing A-type granites, lying on opposite sides of the South Tien Shan suture. *Ore Geology Reviews*, *35*(2), 206–216. https://doi.org/10.1016/j.oregeorev.2009.01.002

Kröner, A., Alexeiev, D. V., Rojas-Agramonte, Y., Hegner, E., Wong, J., Xia, X., . . . Kiselev, V. V. (2013). Mesoproterozoic (Grenville-age) terranes in the Kyrgyz North Tianshan: Zircon ages and Nd-Hf isotopic constraints on the origin and evolution of basement blocks in the southern Central Asian Orogen. *Gondwana Research*, *23*, 272–295. https://doi.org/10.1016/j.gr.2012.05.004

Kröner, A., Kovach, V., Alexeiev, D., Wang, K. L., Wong, J., Degtyarev, K., & Kozakov, I. (2017). No excessive crustal growth in the Central Asian Orogenic Belt: Further evidence from field relationships and isotopic data. *Gondwana Research*, *50*, 135–166. https://doi.org/10.1016/j.gr.2017.04.006

Kröner, A., Kovach, V., Belousova, E., Hegner, E., Armstrong, R., Dolgopolova, A., . . . Sun, M. (2014). Reassessment of continental growth during the accretionary history of the Central Asian Orogenic Belt. *Gondwana Research*, *25*, 103–125. https://doi.org/10.1016/j.gr.2012.12.023

Lanari, P., Riel, N., Guillot, S., Vidal, O., Schwartz, S., Pecher, A., & Hattori, K. H. (2013). Deciphering high-pressure metamorphism in collisional context using microprobe mapping methods: Application to the Stak eclogitic massif (northwest Himalaya). *Geology*, *41*, 111–114. https://doi.org/10.1130/G33523.1

Lanari, P., Vho, A., Bovay, T., Airaghi, L., & Centrella, S. (2018). Quantitative compositional mapping of mineral phases by electron probe micro-analyser. *Geological Society, London, Special Publications*, *478*, SP478-4. https://doi.org/10.1144/SP478.4

Lanari, P., Vidal, O., de Andrade, V., Dubacq, B., Lewin, E., Grosch, E. G., & Schwartz, S. (2014). XMapTools: A MATLAB©-based program for electron microprobe X-ray image processing and geothermobarometry. *Computers & Geosciences*, *62*, 227–240. https://doi.org/10.1016/j.cageo.2013.08.010

Laurent-Charvet, S., Charvet, J., Monié, P., & Shu, L. (2003). Late Paleozoic strike-slip shear zones in eastern central Asia (NW China): New structural and geochronological data. *Tectonics*, *22*, 1009. https://doi.org/10.1029/2001TC901047

Leake, B. E. (1978). Nomenclature of amphiboles. *American Mineralogist*, *63*, 1023–1052.

Li, Q., Lin, W., Su, W., Li, X., Shi, Y., Liu, Y., & Tang, G. (2011). SIMS U-Pb rutile age of low-temperature eclogites from southwestern Chinese Tianshan, NW China. *Lithos*, *122*, 76–86. https://doi.org/10.1016/j.lithos.2010.11.007

Liu, X., Su, W., Gao, J., Li, J., Jiang, T., Zhang, X., & Ge, X. (2014). Paleozoic subduction erosion involving accretionary wedge sediments in the South Tianshan Orogen: Evidence from geochronological and geochemical studies on eclogites and their host metasediments. *Lithos*, *210–211*, 89–110. https://doi.org/10.1016/j.lithos.2014.09.017

Loury, C., Rolland, Y., Cenki-Tok, B., Lanari, P., & Guillot, S. (2016). Late Paleozoic evolution of the South Tien Shan: Insights from P-T estimates and allanite geochronology on retrogressed eclogites (Chatkal range, Kyrgyzstan). *Journal of Geodynamics*, *96*, 62–80. https://doi.org/10.1016/j.jog.2015.06.005

Loury, C., Rolland, Y., Guillot, S., Mikolaichuk, A. V, Lanari, P., Bruguier, O., & Bosch, D. (2015). Crustal-scale structure of South Tien Shan: Implications for subduction polarity and Cenozoic reactivation. In M. F. Brunet, T. McCann & E. R. Sobel (Eds.), *Geological evolution of Central Asian basins and the Western Tien-Shan range*. *Geological Society of London Special Publications*, *427*, 197–229. https://doi.org/10.1144/sp427.4

Loury, C., Rolland, Y., Lanari, P., Guillot, S., Bosch, D., Ganino, C., … Riel, N. (2018). Permian charnockites in the Pobeda area: Implications for Tarim mantle plume activity and HT metamorphism in the South Tien Shan range. *Lithos*, *304*, 135–154. https://doi.org/10.1016/j.lithos.2018.01.025

Lü, Z., Bucher, K., Zhang, L., & Du, J. (2012). The Habutengsu metapelites and metagreywackes in western Tianshan, China: Metamorphic evolution and tectonic implications. *Journal of Metamorphic Geology*, *30*(9), 907–926.

Ma, X., Shu, L., Meert, J. G., & Li, J. (2014). The Paleozoic evolution of Central Tianshan: Geochemical and geochronological evidence. *Gondwana Research*, *25*(2), 797–819. https://doi.org/10.1016/j.gr.2013.05.015

Makarov, V. I., Alekseev, D. V., Batalev, V. Y., Bataleva, E. A., Belyaev, I. V., Bragin, V. D., … Shchelochkov, G. G. (2010). Underthrusting of Tarim beneath the Tien Shan and deep structure of their junction zone: Main results of seismic experiment along MANAS Profile Kashgar-Song-Köl. *Geotectonics*, *44*, 102–126. https://doi.org/10.1134/S0016852110020020

Mark, D. F., Stuart, F. M., & de Podesta, M. (2011). New high-precision measurements of the isotopic composition of atmospheric argon. *Geochimica et Cosmochimica Acta*, *75*, 7494–7501. https://doi.org/10.1016/j.gca.2011.09.042

Massonne, H. J., & Schreyer, W. (1987). Phengite geobarometry based on the limiting assemblage with K-feldspar, phlogopite, and quartz. *Contributions to Mineralogy and Petrology*, *96*, 212–224. https://doi.org/10.1007/BF00375235

McDougall, I., & Harrison, T. M. (1999). *Geochronology and thermochronology by the $^{40}Ar/^{39}Ar$ method* (2nd ed). Oxford, UK: Oxford University Press.

Metcalfe, I. (2013). Gondwana dispersion and Asian accretion: Tectonic and palaeogeographic evolution of eastern Tethys. *Journal Asian Earth Sciences*, *66*, 1–33. https://doi.org/10.1016/j.jseaes.2012.12.020

Meyer, M., Klemd, R., John, T., Gao, J., & Menneken, M. (2016). An (in-) coherent metamorphic evolution of high-P eclogites and their host rocks in the Chinese southwest Tianshan? *Journal of Metamorphic Geology*, *34*, 121–146. https://doi.org/10.1111/jmg.12175

Mikolaichuk, A. V., Kurenkov, S. A., Degtyarev, K. E., & Rubstov, V. I. (1997). Northern Tianshan, main stages of geodynamic evolution in the late Precambrien and early Paleozoic. *Geotectonics*, *31*, 445–462.

Molnar, P., & Tapponnier, P. (1975). Cenozoic tectonics of Asia : Effects of a continental collision. *Science*, *189*(4201), 419–426. https://doi.org/10.1126/science.189.4201.419

Mühlberg, M., Hegner, E., Klemd, R., Pfänder, J. A., Kaliwoda, M., & Biske, Y. S. (2016). Late Carboniferous high-pressure metamorphism of the Kassan Metamorphic Complex (Kyrgyz Tianshan) and assembly of the SW Central Asian Orogenic Belt. *Lithos*, *264*, 41–55. https://doi.org/10.1016/j.lithos.2016.08.008

Nikolaev, V. A. (1933). About principal structural line of Tian Shan. *Proceedings of All-Russian Mineralogical Society, Series*, *2*(62), 347–354 (in Russian).

Pearce, J. A. (2008). Geochemical fingerprinting of oceanic basalts with applications to ophiolite classification and the search for Archean oceanic crust. *Lithos*, *100*, 14–48. https://doi.org/10.1016/j.lithos.2007.06.016

Ravna, E. J. (2000). The garnet – clinopyroxene Fe^{2+} – Mg geothermometer: An updated calibration. *Journal of Metamorphic Geology*, *18*(2), 211–219. https://doi.org/10.1046/j.1525-1314.2000.00247.x

Rojas-Agramonte, Y., Kröner, A., Alexeiev, D. V., Jeffreys, T., Khudoley, A. K., Wong, J., … Kiselev, V. V. (2014). Detrital and igneous zircon ages for supracrustal rocks of the Kyrgyz Tianshan and palaeogeographic implications. *Gondwana Research*, *26*, 957–974. https://doi.org/10.1016/j.gr.2013.09.005

Rolland, Y., Alexeiev, D. V., Kröner, A., Corsini, M., Loury, C., & Monié, P. (2013). Late Palaeozoic to Mesozoic kinematic history of the Talas-Ferghana strike-slip fault (Kyrgyz West Tianshan) as revealed by 40Ar/39Ar dating of syn-kinematic white mica. *Journal of Asian Earth Sciences*, *67–68*, 76–92. https://doi.org/10.1016/j.jseaes.2013.02.012

Rolland, Y., Lardeaux, J. M., Guillot, S., & Nicollet, C. (2000). Extension syn-convergence, poinçonnement vertical et unités métamorphiques contrastées en bordure ouest du Grand Paradis (Alpes Franco-Italiennes). *Geodinamica Acta*, *13*(2–3), 133–148.

Rudnick, R. L., & Gao, S. (2003). Composition of the continental crust. In H. D. Holland & K. K. Turekian (Eds.), *Treatise on geochemistry* (pp. 1–64). Volume 3. New York: Elsevier. https://doi.org/10.1016/B0-08-043751-6/03016-4.

Sanchez, G., Rolland, Y., Schneider, J., Corsini, M., Oliot, E., Goncalves, P., … Marquer, D. (2011). Dating low-temperature deformation by $^{40}Ar/^{39}Ar$ on white mica, insights from the Argentera-Mercantour Massif (SW Alps). *Lithos*, *125*(1), 521–536. https://doi.org/10.1016/j.lithos.2011.03.009

Sang, M., Xiao, W., Bakirov, A., Orozbaev, R., Sakiev, K., & Zhou, K. (2016). Oblique wedge extrusion of UHP/HP complexes in the Late Triassic: Structural analysis and zircon ages of the Atbashi Complex, South Tianshan, Kyrgyzstan. *International Geological Reviews*, *59*(10), 1369–1389.

Sang, M., Xiao, W., Orozbaev, R., Bakirov, A., Sakiev, K., Pak, N, … Zhang, Z. (2017). Structural styles and zircon ages of the South Tianshan accretionary complex, Atbashi Ridge, Kyrgyzstan: Insights for the anatomy of ocean plate stratigraphy and accretionary processes. *Journal of Asian Earth Sciences*, *153*, 9–41. https://doi.org/10.1016/j.jseaes.2017.07.052

Schwartz, S. (2000). *La zone piémontaise des Alpes occidentales : un paléo-complexe de subduction. Arguments métamorphiques, géochronologiques et structuraux*. PhD thesis, Université Claude-Bernard-Lyon I.

Seltmann, R., Konopelko, D., Biske, G., Divaev, F., & Sergeev, S. (2011). Hercynian post-collisional magmatism in the context of Paleozoic magmatic evolution of the Tien Shan orogenic belt. *Journal of Asian Earth Sciences*, *42*(5), 821–838. https://doi.org/10.1016/j.jseaes.2010.08.016

Sengör, A. M. C., Natalin, B. A., & Burtman, V. S. (1993). Evolution of the Altaid tectonic collage and Palaeozoic crustal growth in Eurasia. *Nature*, *364*, 299–307. https://doi.org/10.1038/364299a0

Simonov, V. A., Sakiev, K. S., Volkova, N. I., Stupakov, S. I., & Travin, A. V. (2008). Conditions of formation of the Atbashi Ridge eclogites (South Tien Shan). *Russian Geology and Geophysics*, *49*, 803–815. https://doi.org/10.1016/j.rgg.2008.04.001

Sobel, E. R., Oskin, M., Burbank, D., & Mikolaichuk, A. (2006). Exhumation of basement-cored uplifts: Example of the Kyrgyz Range quantified with apatite fission track thermochronology. *Tectonics*, *25*, TC2008. https://doi.org/10.1029/2005TC001809

Soldner, J., Oliot, E., Schulmann, K., Štípská, P., Kusbach, V., & Anczkiewicz, R. (2017). Metamorphic P-T-t-d evolution of (U)HP metabasites from the South Tianshan accretionary complex (NW China) – Implications for rock deformation during exhumation in a subduction channel. *Gondwana Research*, *47*, 161–187. https://doi.org/10.1016/j.gr.2016.07.007

Sorensen, S. S. (1988). Petrology of amphibolite-facies mafic and ultramafic rocks from the Catalina Schist, southern California: Metasomatism and migmatization in a subduction zone metamorphic setting. *Journal of Metamorphic Geology*, *6*, 405–435. https://doi.org/10.1111/j.1525-1314.1988.tb00431.x: 405-435

Spear, F. S. (1995). *Metamorphic phase equilibria and pressure-temperature-time paths*. Washington, DC: Mineralogical Society of America.

Su, W., Gao, J., Klemd, R., Li, J.-L., Zhang, X., Li, X.-H., … Zhang, L. (2010). U-Pb zircon geochronology of Tianshan eclogites in NW China: Implication for the collision between the Yili and Tarim blocks of the southwestern Altaids. *European Journal of Mineralogy*, *22*(4), 473–478. https://doi.org/10.1127/0935-1221/2010/0022-2040

Sun, S.-S., & McDonough, W. F. (1989). Chemical and isotopic systematics of oceanic basalts: Implications for mantle composition and processes. *Geological Society London Special Publications*, *42*, 313–345. https://doi.org/10.1144/GSL.SP.1989.042.01.19

Tagiri, M., Yano, T., Bakirov, A., Nakajima, T., & Uchiumi, S. (1995). Mineral parageneses and metamorphic P-T-t paths of ultrahigh-pressure eclogites from Kyrghyzstan Tien-Shan. *Island Arc*, *4*, 280–292. https://doi.org/10.1111/j.1440-1738.1995.tb00150.x

Tian, Z. L., & Wei, C. J. (2013). Metamorphism of ultrahigh-pressure eclogites from the Kebuerte Valley, South Tianshan, NW China: Phase equilibria and P-T path. *Journal of Metamorphic Geology*, *31*(3), 281–300. https://doi.org/10.1111/jmg.12021

Tricart, P., & Schwartz, S. (2006). A north-south section across the Queyras Schistes lustrés (Piedmont zone, Western Alps): Syn-collision refolding of a subduction wedge. *Eclogae Geologicae Helvetiae*, *99*, 429–442. https://doi.org/10.1007/s00015-006-1197-6

Tursungaziev, B. T., & Petrov, O. V. (2008). *Geological map of Kirghyz republic, scale 1:500000*. Saint-Petersbourg, Russia: VSEGEI (in Russian).

Udovkina, N. G. (1985). *Eclogites of the USSR*. Moscow, Russia: Nauka (in Russian).

Uunk, B., Brouwer, F., ter Voorde, M., & Wijbrans, J. (2018). Understanding phengite argon closure using single grain fusion age distributions in the Cycladic Blueschist Unit on Syros, Greece. *Earth and Planetary Science Letters*, *484*, 192–203. https://doi.org/10.1016/j.epsl.2017.12.031

van der Straaten, F., Schenk, V., John, T., & Gao, J. (2008). Blueschist-facies rehydration of eclogites (Tian Shan, NW-China): Implications for fluid–rock interaction in the subduction channel. *Chemical Geology*, *255*, 195–219. https://doi.org/10.1016/j.chemgeo.2008.06.037

Vidal, O., de Andrade, V., Lewin, E., Munoz, M., Parra, T., & Pascarelli, S. (2006). P-T-deformation-Fe^{3+}/Fe^{2+} mapping at the thin section scale and comparison with XANES mapping: Application to a garnet-bearing metapelite from the Sambagawa metamorphic belt (Japan). *Journal of Metamorphic Geology*, *24*, 669–683. https://doi.org/10.1111/j.1525-1314.2006.00661.x

Vidal, O., Parra, T., & Vieillard, P. (2005). Thermodynamic properties of the Tschermak solid solution in Fe-chlorite: Application to natural examples and possible role of oxidation. *American Mineralogist*, *90*, 347–358. https://doi.org/10.2138/am.2005.1554

Villa, I. M. (2015). ^{39}Ar-^{40}Ar geochronology of mono-and polymetamorphic basement rocks. *Periodico di mineralogia*, *84*(3b), 615–632.

Wang, B., Chen, Y., Zhan, S., Shu, L., Faure, M., Cluzel, D., … Laurent-Charvet, S. (2007). Primary Carboniferous and Permian paleomagnetic results from the Yili Block (NW China) and their implications on the geodynamic evolution of Chinese Tianshan Belt. *Earth and Planetary Science Letters*, *263*, 288–308. https://doi.org/10.1016/j.epsl.2007.08.037

Wang, B., Cluzel, D., Shu, L., Faure, M., Charvet, J., Chen, Y., … Jong, K. (2009). Evolution of calc-alkaline to alkaline magmatism through Carboniferous convergence to Permian transcurrent tectonics, western Chinese Tianshan. *International Journal of Earth Sciences*, *98*, 1275–1298. https://doi.org/10.1007/s00531-008-0408-y

Wang, B., Zhai, Y., Kapp, P., de Jong, K., Zhong, L., Liu, H., … Geng, H. (2017). Accretionary tectonics of back-arc oceanic basins in the South Tianshan: Insights from structural, geochronological, and geochemical studies of the Wuwamen ophiolite mélange. *Geological Society of America Bulletin*, *130*(1-2), 284–306. https://doi.org/10.1130/B31397.1

Warren, C. J., Hanke, F., & Kelley, S. P. (2012). When can muscovite $^{40}Ar/^{39}Ar$ dating constrain the timing of metamorphic exhumation? *Chemical Geology*, *291*, 79–86. https://doi.org/10.1016/j.chemgeo.2011.09.017

Waters, D. J. (1996). The Garnet-Cpx-Phengite barometer. Recommended calibration and calculation method, updated 1 March 1996. http://www.earth.ox.ac.uk/davewa/research/eclogites/ecbarcal.html

Waters, D. J., & Martin, H. N. (1993). Geobarometry of phengite-bearing eclogites. *Terra Abstracts*, *5*, 410–411.

Whitney, D. L., & Evans, B. W. (2010). Abbreviations for names of rock-forming minerals. *American Mineralogist*, *95*, 185–187. https://doi.org/10.2138/am.2010.3371

Wilhem, C., Windley, B. F., & Stampfli, G. M. (2012). The Altaids of Central Asia: A tectonic and evolutionary innovative review. *Earth-Science Reviews*, *113*(3), 303–341. https://doi.org/10.1016/j.earscirev.2012.04.001

Windley, B. F., Alexeiev, D. V. V., Xiao, W., Kroner, A., & Badarch, G. (2007). Tectonic models for accretion of the Central Asian Orogenic Belt. *Journal of the Geological Society London*, *164*, 31–47. https://doi.org/10.1144/0016-76492006-022

Windley, B. F., Allen, M. B., Zhang, C., Zhao, Z.-Y., & Wang, G.-R. (1990). Paleozoic accretion and Cenozoic redeformation of the Chinese Tien Shan Range, central Asia. *Geology*, *18*, 128. https://doi.org/10.1130/0091-7613(1990) 018<0128:PAACRO>2.3.CO;2

Xiao, W., Huang, B., Han, C., Sun, S., & Li, J. (2010). A review of the western part of the Altaids: A key to understanding the architecture of accretionary orogens. *Gondwana Research*, *18*, 253–273. https://doi.org/10.1016/j.gr.2010.01.007

Xiao, W., Windley, B., Sun, S., Li, J., Huang, B., Han, C., . . . Chen, H. (2014). A tale of amalgamation of three Permo-Triassic Collage Systems in Central Asia: Oroclines, sutures, and terminal accretion. *Annual Reviews in Earth and Planetary Sciences*, *43*, 150504155237007. https://doi.org/10.1146/annurev-earth-060614-105254

Yang, X., Zhang, L. F., Tian, Z. L., & Bader, T. (2013). Petrology and U-Pb zircon dating of coesite-bearing metapelite from the Kebuerte Valley, western Tianshan, China. *Journal of Asian Earth Sciences*, *70–71*, 295–307. https://doi.org/10.1016/j.jseaes.2013.03.020

Zhong, L. L., Wang, B., Alexeiev, D. V., Cao, Y. C., Biske, S. Y., Liu, H. S., . . . Langzhang, X. (2017). Paleozoic multi-stage accretionary evolution of the SW Chinese Tianshan: New constraints from plutonic complex in the Nalati Range. *Gondwana Research*, *45*, 254–274. https://doi.org/10.1016/j.gr.2016.12.012

SUPPORTING INFORMATION

Additional supporting information may be found online in the Supporting Information section at the end of the article.

Appendix S1. Sampling and analytical procedures.

Table S1. List of names, locations, types and units of samples analysed in this study.

Figure S1. CaO compositional maps of the studied sample.

Figure S2. Map of jadeite content in omphacite showing the complex zonation pattern of grains included in garnet.

Table S2. Acquisition parameters of each X-ray map.

Table S3. Chemical compositions of garnet (in oxide wt%) and structural formulae (p.f.u.).

Table S4. Chemical compositions of clinopyroxene (in oxide wt%) and structural formulae (p.f.u.).

Table S5. Chemical compositions of amphibole (in oxide wt%) and structural formulae (p.f.u.).

Table S6. Chemical compositions of phengite (in oxide wt%) and structural formulae (in pfu).

Table S7. Chemical compositions (in oxides wt%) of the present garnet and matrix calculated from the small map, and calculated Local Bulk Composition (LBC).

Table S8. Representative chemical compositions (in oxide wt.%) of HP meta-sedimentary unit (sample KG-12-50) garnet and corresponding structural formulae.

Table S9. Representative chemical compositions (in oxide wt.%) of white mica and corresponding atom site distribution calculated on a 11 anhydrous oxygen basis.

Table S10. Representative chemical compositions (in oxide wt.%) of chlorite and corresponding structural formulae calculated on a 14 anhydrous oxygen basis.

Table S11. Representative chemical compositions (in oxide wt.%) of amphibole and corresponding structural formulae.

Table S12. Representative chemical compositions of Accretionary prism (metabasite) epidote and corresponding structural formulae.

Table S13. Representative chemical compositions (in oxide wt.%) of pyroxene from the Accretionary prism (metabasite) and corresponding structural formulae.

Table S14. Chemical compositions of HPMU and of Accretionary prism unit blueschists.

Table S15. RSCM thermometry Results. T_{max} is calculated following the method of Beyssac et al. (2002a), n is the number of analyzed graphite grains, SD: standard deviation, SE: standard error (1σ).

Figure S3. Raman spectra of carbonaceous material of the HPMU samples. The grey area represents the spectra of the accretionary prism samples after Jourdon et al. (2017a).

Figure S4. *P-T* diagram showing mica-quartz-water equilibria depending on aH_2O values. Phengite analyses from sample KG− 12− 64 are used.

Table S16. Results of $^{40}Ar/^{39}Ar$ step-heating experiments.

How to cite this article: Loury C, Rolland Y, Guillot S, et al. Tectonometamorphic evolution of the Atbashi high-*P* units (Kyrgyz CAOB, Tien Shan): Implications for the closure of the Turkestan Ocean and continental subduction–exhumation of the South Kazakh continental margin. *J Metamorph Geol*. 2018;36:959–985. https://doi.org/10.1111/jmg.12423